Bulk mineralogy of Lunar crater central peaks via thermal infrared spectra from the Diviner Lunar Radiometer - A study of the Moon's crustal composition at depth

Eugenie Song

A thesis submitted in partial fulfillment of the requirements for the degree of

Master of Sciences

University of Washington

2012

Committee:

Joshua Bandfield

Alan Gillespie

Bruce Nelson

Program Authorized to Offer Degree:
Earth and Space Sciences

Table of Contents

List of Figures

List of Tables

University of Washington

Abstract

Bulk mineralogy of Lunar crater central peaks via thermal infrared spectra from the Diviner Lunar Radiometer - A study of the Moon's crustal composition at depth

Eugenie Song

Chair of the Supervisory Committee:
Dr. Joshua Bandfield
Earth and Space Sciences

The central peaks of lunar impact craters are thought to be composed of uplifted material originating from varying depths of the crustal column. The crystallization sequence of the early lunar magma ocean resulted in an anorthositic upper crust that becomes progressively more mafic as it approaches the olivine-rich mantle. Emissivity spectra centered around 8 microns from the Lunar Reconnaissance Orbiter (LRO) Diviner Radiometer are used to derive the wavelength location of the Christiansen Feature (CF), which is sensitive to bulk silicate mineralogy. A survey of CF values has been performed for the central peaks of 135 complex craters, providing global and regional observations of the heterogeneity of crustal compositions. Crustal thickness models give context to the pre-impact depth of the central peak material and its proximity to the crust-mantle boundary. The bulk composition results were also compared to central peak FeO abundance and optical maturity parameters (both derived from Clementine Ultraviolet/Visible camera data) to better understand spectral behavior in the 8 μm region due to varying surface properties. This study has identified 6 craters with potentially ultramafic regions on their central peaks. More common occurrences of mafic material, found in a wide variety of crater central peaks, show a silicate composition with a mafic component similar to mare basalt. The compositional distribution and variety of the 135 craters is similar to that of the rest of the Moon, which implies that uplifted material found in the central peaks is not significantly different from the range of compositions found on the lunar surface. Bulk composition of the central peak material does not appear to be correlated with its crustal depth of origin, suggesting both lateral and vertical heterogeneity in crustal composition rather than a gradual transition from felsic to mafic composition. It is likely that the Moon's extensive cratering history has continually overturned the original crust, erasing the stratigraphic sequence caused by cooling of the global magma ocean.

1 Introduction

1.1 Formation of the Lunar Crust

The modern lunar crust is a product of two highly energetic and interactive processes – the melting and subsequent crystallization of magma bodies over a wide range of scales that has created a crust of diverse silicate lithologies and the persistent barrage of crater forming impacts that pulverize, overturn, and uplift the crust and its existing stratigraphy. Studies of terrestrial craters and Apollo samples along with sophisticated modeling of the Moon's formation and crustal evolution have provided a framework of how and when these processes occurred [*Heiken et al.*, 1991; *Jolliff et al.*, 2006].

The prevailing explanation for lunar formation is the Giant Impact hypothesis where a Mars-sized body obliquely impacted the proto-Earth shortly after the origin of the solar system ~4.5 billion years ago [*Heiken et al.,* 1991]. The off-center impact obliterated the impactor leaving much of its heavier components like iron to be incorporated into the Earth's core. The remaining debris reaccreted to form the Moon, with at least the outer several hundred kilometers being molten, forming a global magma ocean. As the magma ocean cooled, fractional crystallization occurred to create a vertically heterogeneous crust.

Based on the crystallization sequence of the magma ocean, the cumulate layers are thought to be largely olivine at the crust-mantle interface with increasing proportions of orthopyroxene and clinopyroxene as they approach the surface. After about 70% of the magma ocean had crystallized, the aluminum content of the melt had increased enough to permit plagioclase saturation, and the high density of the residual magma allowed for lower density plagioclase minerals to form a floating anorthositic crust. In the Apollo collection, diverse mafic coarse-crystalline rocks indicate that plutons formed at shallow depths within the crust. The generally higher ratio of Mg to the sum of Mg and Fe of these rocks have led them to be referred to as the "Mg-suite"[*Warner et al.,* 1976]. Because the crust as a whole is more mafic than the known anorthosites, as much as 20% of the crust by volume could be composed of Mg-suite rocks or other mafic components.

Massive impacts during the Late Heavy Bombardment (~4.1-3.8 Gya) created numerous large basins. Basalt formed by the remelting of the mafic cumulates from earlier stages of magma ocean differentiation flooded most of the basins, creating the darker mare terrain (3.9-3.1 Gya) [*BVSP*, 1981]. Cratering continued at a decreased rate, resulting in a variety of crater types on its surface. Owing to the lack of atmosphere, few changes occurred that are not related to cratering. Today's lunar regolith is a poorly consolidated layer generated from the constant meteoroid interactions with the bedrock [*Hörz et al.*, 1991].

Using telescopic near-IR spectroscopy, *Pieters* [1986]showed that the ejecta deposits small craters that sample the upper kilometer of the lunar crust are relatively uniform in composition, probably because the surface has been exposed to intense mixing from impacts. To view the lunar crust below this mixed layer, Pieters studied the central peaks of large craters, which are composed of uplifted crustal material and expose rock originating from varying depths of the lunar subsurface. Since the study of *Pieters* [1986], *Tompkins and Pieters* [1999] used visible and near-IR multispectral imaging obtained from lunar orbit to examine many more craters, and distributed locally, to demonstrate the compositional diversity of the lunar crust.

Until recently, visible and near-IR spectroscopy remained the only data available to study a large sample of central peaks. However, the Diviner radiometer collected (and continues to collect) multispectral imaging in the region of thermal emission near 8 microns that contains information complementary to that revealed by near-IR data. Thermal multispectral imaging is especially sensitive to the ratio of feldspar to mafic minerals, which is crucial to understanding the basic lithology of lunar rocks but difficult to extract from near-IR data.

The focus of this study is to understand the distribution of deep seated crustal and potentially mantle-sourced material within the uplifted rock in crater central peaks using thermal IR multispectral imaging. In the crystallization sequence described above, the crust becomes more mafic as it approaches the crust-

mantle boundary, assuming that the crustal column is largely preserved throughout the extensive cratering events that occurred after crust formation.

1.2 Crater Morphology

Understanding both the composition of the central peak as well as the depth the uplifted material originated from can be useful in mapping the vertical heterogeneity of the lunar crust, giving insight into the processes involved in lunar crust formation [*Cahill et al.*, 2009; *Cintala and Grieve*, 1998]. The uplifted peak's bulk composition should theoretically become more mafic as its depth of origin approaches the olivine-rich mantle. In this study, central peak bulk composition is determined for 135 craters with diameters ranging from 26 km to almost 200km, providing a look at the range of felsic and mafic compositions originating from a variety of crustal depths across the globe.

Crater morphology is strongly correlated with the diameter of the crater, with central peak formations typically occurring in craters with diameters between ~20-140km [*Melosh*, 1989]. Terrestrial studies of complex craters have shown that the material making up the central peak is uplifted rock that originated below the floor of the crater [*Grieve and Robertson*, 1979; *Grieve*, 1981]. The initial stage of a complex crater is bowl-shaped but gravitationally unstable – this is the transient crater that forms immediately after impact [*Melosh and Ivanov*, 1999]. The walls of the transient crater begin to collapse under gravitational forces and the shock wave resulting from this collapse produces the characteristic central uplift. These impact events are intensely high-energy, and the uplift of material can originate from depths of tens of kilometers in the crust [*Wieczorek and Zuber*, 2001]. The depth of origin of the uplifted central peak material is a function of crater diameter, where large craters are uplifting from a greater depth than small craters. Like in *Cahill et al.* [2009], this study assumes the minimum depth of origin coincides with the maximum depth of melting, which is $0.108 \times Crater\ Diameter^{0.98}$ [*Cintala and Grieve*, 1998].

1.3 Spectral Features of Rock-Forming Silicates in the Lunar Environment

99% of lunar rocks are composed of four minerals - plagioclase, pyroxene, olivine, and ilmenite [*Lucey et al.*, 2006]. Spectral features of silicate minerals occur in the mid-infrared region of the spectrum between ~8-12 µm, where Si-O bonds within crystal structures are asymmetrically stretched through interaction with incident photons resulting in a fundamental molecular vibration. The strength and wavelength location of the absorption feature is dependent on the structure and cation makeup of the silicate crystal. There are also local factors such as ambient pressure and grain size that can change the effective opacity of the observed surface [*Estep-Barnes*, 1977]. For powders in a vacuum, like on the Moon, these silicate optical properties are expressed as an emission peak known as the Christiansen Feature (CF).

Table 1 Common Lunar silicate minerals - their molecular structures [*Estep-Barnes*, 1977] *and CF positions* [*Greenhagen et al.*, 2010].

Mineral	Silicate Class	Degree of Polymerization	Molecular Grouping	Si:O Ratio	CF Position
Olivine	nesosilicate	single tetrahedral	SiO_4^{4-}	Si : O = 0.25	8.67µm (forsterite endmember)
Pyroxene	inosilicate	single chain	SiO_3^{2-}	Si : O = 0.33	8.25µm (intermediate composition)
Plagioclase	tectosilicate	framework	SiO_2	Si : O = 0.50	7.84µm (anorthite endmember)

The strongest fundamental Si-O vibrational modes of these minerals form absorption features between 8-12 µm that shift towards shorter wavelengths as the lattice bond strength increases [*Kahle et al.*, 1993]. The CF occurs in the 7.5-9.0 µm wavelength range for silicates and is an emissivity maximum at wavelengths just shortward of the fundamental absorption features. The wavelength location of this maximum is shifted based on the degree of polymerization of silicates [Table 1] and thus can be an indicator of bulk mineralogy. The degree of silica polymerization is directly related to the composition of the magma and the temperatures they formed in (resulting in varying stages of fractional crystallization of a magma ocean).

The CF emissivity peak has shown to become more pronounced in a simulated lunar environment, as well as systematically shifted towards shorter wavelengths [*Salisbury*, 1993]. The CF occurs as the wavelength-dependent refractive index of the mineral grains undergoes anomalous dispersion and asymptotically decreases just prior to a fundamental molecular vibration band, where it approaches the refractive index of the surrounding environment. This minimizes reflection at grain boundaries, and absorption is relatively low because of its proximity to the Reststrahlen feature flank. At the wavelength location of the CF, radiation can pass through the sample relatively freely [*Mustard and Hays*, 1997].

1.4 Compositional Studies of Lunar Crater Central Peaks

Previous studies of central peak compositions have utilized data from telescopic instruments [*Lucey et al.*, 1991; *Pieters*, 1982, 1986] and lunar orbiting near-infrared (NIR) multi and hyperspectral instruments (e.g. Clementine UVVIS-NIR, Kaguya Spectral Profiler, Moon Mineralogy Mapper). The diagnostic mafic mineral absorption features seen in NIR spectroscopy has proven extremely useful for identifying a diverse range of mineralogies within central peaks [*Cahill et al.*, 2009; *Tompkins and Pieters*, 1999].

Tompkins and Pieters [1999] derived central peak compositions of 109 craters using Clementine UVVIS multispectral data (5 bands ranging from 0.4 - 1.0 μm). Two spectral parameters were used for classification - "key ratio", a band ratio that estimates the relative abundance of mafic minerals, and "spectral curvature", the angle formed between the longer wavelength bands to distinguish between mafic minerals - particularly pyroxene composition. Laboratory spectra of various mixtures of mineral end-members (olivine, orthopyroxene, clinopyroxene, anorthosite) were convolved with Clementine filters for comparison to the lunar data, allowing for estimation of the mineral abundances based on the two spectral parameters.

Global trends in *Tompkins and Pieters* [1999] study showed that the highlands crater peaks are generally composed of gabbroic, noritic, or troctolitic anorthosite (85-90% plagioclase). Peaks of craters in or around basins are mostly comprised of anorthositic norite and a wider range of gabbroic, noritic, or

troctolitic anorthosite (80-90% plagioclase). Basin craters also more frequently exhibited multiple lithologies. The 6 craters found with troctolitic compositions also contain anorthosite in their central peaks. This study found clear evidence for compositional heterogeneity in the crust and differing proportions of mafic rock types within highlands and basin craters, but there appear to be no distinct vertical or lateral patterns in the suite of craters examined.

The compositional analysis from *Tompkins and Pieters* [1999] was expanded to include comparisons to a dual-layered crustal thickness model by *Wieczorek and Zuber* [2001]. The model is based on the assumption that the lunar crust is stratified into an anorthositic upper layer and noritic lower layer, where much of the crustal thickness variation occurs within the upper layer. Based on central peak composition and depth of origin, the upper crust is composed of 88±4 vol.% plagioclase and the most mafic lower crust contains 65±8 vol.% plagioclase, which is more felsic than typical mare basalt with ~20-40 vol.% plagioclase [*BVSP*, 1981]. The study concludes that both the upper and lower crust could have formed by cumulate flotation in a magma ocean due to the high plagioclase content of both layers that would maintain buoyancy of the cumulate assemblage.

Cahill et al [2009] targeted 55 craters that are possibly excavating lower crust and/or mantle material in their central peaks using the approach of *Wieczorek and Zuber* [2001] and combined compositional modeling derived from Clementine UVVIS and NIR spectra (8 bands between 0.75 - 2.0 μm) with depth of origin models to analyze crustal composition with depth. Clementine spectra were compared to modeled spectra based on radiative transfer theory, mineral optical constant data, and iron optical constant data in order to determine the proportions of olivine, orthopyroxene, clinopyroxene, and plagioclase in the peaks. The depth of origin of central peak material (a function of crater diameter) was combined with a single-layer crustal thickness model to compare each crater's central peak composition with its depth of origin relative to the crust-mantle interface. About half of the craters investigated are calculated to have plausibly uplifted material from within 5km of the crust-mantle interface. The results of this work show a

large diversity of lithologies in both terrains, with the majority of peaks consisting of mafic composition similar to Mg-suite rocks.

Peaks with mafic lithologies were generally located in the South-Pole Aitken and Procellarum KREEP Terranes within 50 km of the crust-mantle boundary. This is consistent with a crust with increasingly mafic mineralogy as it approaches the mantle, although these mafic peaks are also confined to regions with relatively low crustal thicknesses. Anorthositic peaks were largely confined to the highlands but appeared throughout the crustal column, which is inconsistent with a simple increasingly mafic crust with depth [*Ryder and Wood*, 1977] and suggests a more complex formation mechanism.

NIR hyperspectral data from the Spectral Profiler onboard the Kaguya orbiter were used to identify olivine-rich exposures located in concentric regions around SPA, Imbrium, and Moscoviense impact basins where the crust is thin [*Yamamoto et al.*, 2010]. Small, fresh craters on the central peaks of these impact basins commonly expose the olivine-rich spots. They propose that the olivine can be attributed to Mg-rich plutons or excavation of the mantle during the basin forming impacts.

In *Cahill et* al [2009], Copernicus crater was found to contain the highest olivine abundance with 72 vol.% olivine (troctolite). *Tompkins and Pieters* [1999] classified portions of the Copernicus peak as gabbroic, noritic, or troctolitic anorthosite (80-90% plagioclase) and anorthositic troctolite. *Yamamoto et al* [2010] designated the peak and terraces of Copernicus to be olivine rich, as well as Eratosthenes (peak and wall) and Aristarchus (terrace and wall) craters that also surround Imbrium basin.

Several studies identified olivine in NIR spectra of Copernicus crater's central peak as well as three small areas in the northern crater walls [*Lucey et al.*, 1991; *Le Mouélic and Langevin*, 2001; *Pinet et al.*, 1993]. The inner walls of complex craters are terraced due to rim collapse near the end of crater formation, so the walls of the terraces may expose crustal stratigraphy down to the depth of the crater but they are not uplifted in the same manner as central peaks [*Melosh*, 1989].

Emission spectra from the Diviner thermal radiometer, used in this study, offer a complementary spectral window to derive central peak composition. Diviner's CF value is sensitive to bulk silicate mineralogy that can help clarify ambiguities in mineral abundances determined by NIR data [*Lucey and Greenhagen,* 2012], while NIR spectroscopy enhances the interpretation of the CF data, allowing bulk composition to be parsed into the individual minerals present in the mixture. *Greenhagen et al.* [2010] showed an analysis of the global distribution of CF values from Diviner data and identifies exposures of ultra-silica-rich soils at ~1 km resolution. They found no evidence of ultramafic and potentially mantle-sourced material found. Our survey focuses on locating this material specifically within complex craters at ~0.25 km resolution in order to better understand the distribution of mafic minerals throughout the crustal column.

2 Data and Methods

2.1 Diviner Instrument and Data Acquisition

Diviner is a multispectral pushbroom radiometer launched in 2009 onboard the Lunar Reconnaissance Orbiter (LRO). It has nine spectral channels - channels 1 and 2 measure broadband reflected solar radiation between 0.35-2.8 μm, channels 3-9 measure emitted thermal radiation from 7.5-400 μm. The three shortest thermal infrared channels (3-5) have narrow passbands centered around the 8 μm region where the CF occurs for most lunar compositions: 7.55-8.05 μm, 8.10-8.40 μm, and 8.38-8.68 μm. Each of the 9 channels is composed of 21 element linear arrays of 240 μm x 480 μm pixels with a ground resolution of ~160 m (cross-track) by 320 m (in-track) from a 50 km polar orbit. Local times drift by ~2 hours each mapping cycle of Diviner observation [*Paige et al.*, 2009, 2010].

Each Diviner RDR measurement includes the latitude and longitude location at the center of each detector’s instantaneous field of view (FOV). The effective FOV is broadened due to spacecraft movement during the 128ms sample integration time. The broadening occurs in the in-track direction that can be rotated slightly relative to north depending on spacecraft orientation. In order to describe the full

spatial extent of the smeared data point a 2-dimensional Monte Carlo routine generates a specified number of additional data points located randomly within the bounding box of the effective FOV. These points have identical data fields as the original point with the exception of their latitude and longitude locations, so they are able to populate adjacent bins within a rectangular grid that overlap with the full extent of the effective FOV.

The Diviner Level 1b radiance data used in this study was collected from August 28, 2009 through September 26, 2011 (available via Planetary Data System http://pds.nasa.gov/). Data were restricted to local times between 1000 and 1400 to avoid severe illumination conditions that can cause the CF position to shift. Two quality flags from the Diviner RDR were utilized - activity flag = 110 (standard nadir) and quality flag for calibration = 0 (best quality data, calibration marker occurs within nominal time difference from a calibration point). A full description of standard Diviner data processing is available in the Diviner RDR and derived products Software Interface Specification (SIS) version 1.11.

2.2 Data Processing

For each Level 1b data point, the Diviner measurement's footprint is projected by locating the FOV onto a digital elevation model (DEM) from the Lunar Orbiter Laser Altimeter (LOLA) onboard LRO [*Zuber et al.*, 2010]. 2000 additional points per measurement that define the boundary of the effective FOV are added to the data stream to be further processed with the rest of the data. The original data and the new points are projected a final time onto the LOLA DEM to provide target latitude and longitude for every point that is then ready to be binned. These processing steps are crucial for reducing artifacts caused by between-band misregistration and small-scale topographic variation in the final CF maps. The Level 2 Gridded Data Records (GDR) undergo the same processing steps, but with slight variations on the number of additional points for footprint adjustment.

Following geometric and footprint corrections, calibrated radiance data field from channels 3-5 were binned at 128 pixels per degree (~230m per pixel at the equator) and brightness temperatures were

calculated for each band based on a look-up table. The peak of a parabola fit to the 3-point brightness temperature spectrum is assumed to be surface kinetic temperature. The ratio of measured radiance in each band to the calculated radiance at the surface temperature provides an effective emissivity spectrum. CF values were determined by fitting a parabola to the 3-point apparent emissivity spectrum and finding the wavelength at the maximum of the parabola [Fig. 1] [*Glotch et al.*, 2010; *Greenhagen et al.*, 2010 - see supporting online material].

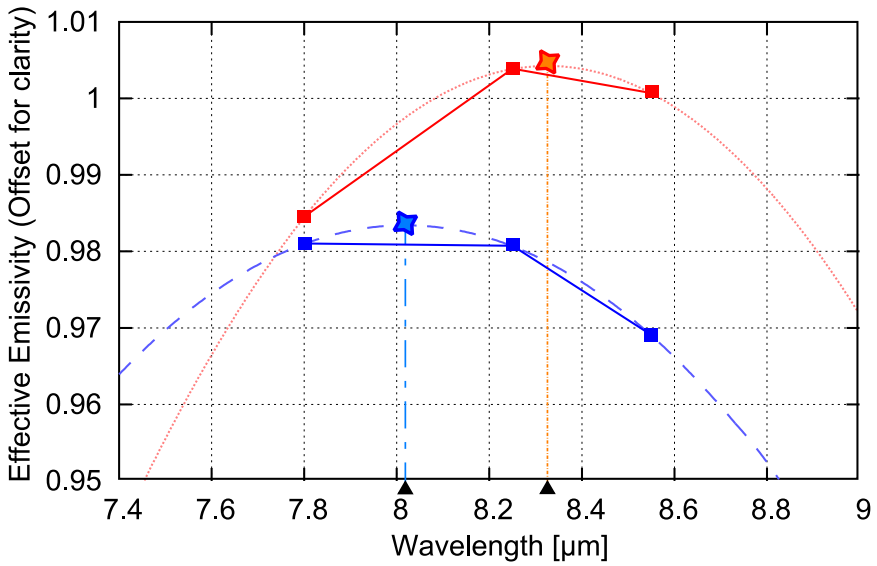

Figure 1 Use of a parabolic fit to 3-point Diviner (7.80 μm, 8.25 μm, 8.55 μm) emissivity spectra to locate Christiansen Feature emissivity maximum. The red trace is an example of a predominantly mafic composition, uplifted in the central peak of Barringer crater where the CF value - the interpolated emissivity maximum - occurs at 8.36 μm. The blue trace is from a more felsic region near the south wall of the same crater, with a CF value of 8.02 μm.

2.3 Anomalous CF shifts

Several properties other than bulk composition shift the wavelength location of the CF in the lunar environment. Although the controlling processes for some of these effects are not fully characterized, they have been isolated and the magnitude of their effect on the CF has been quantified. Data that were clearly dominated by these effects were discarded or masked out.

2.3.1 Anisothermality

The FOV of a single observation always contains a range of temperatures - a phenomenon called anisothermality. The rough lunar surface contains a distribution of solar incidence angles within the measurement FOV due to surface topography primarily at millimeter scales [*Shepard et al.,* 1995]. The brightness temperature measured in each footprint is the weighted average of the temperatures present. The resultant radiance spectrum, a combination of Planck radiance curves for the mixture of temperatures within the FOV, is skewed heavily towards the warmer temperature member present such that the measured brightness temperature will lie somewhere between the average temperature and the highest temperature. The magnitude of skew in the spectrum towards the warmer temperatures in the FOV is highly non-linear and more significant at shorter wavelengths [*Colwell and Jakosky*, 2002; *Smith*, 1967; *Spencer*, 1990].

If emissivity is derived assuming a single temperature, anisothermality introduces a negative slope to the effective emissivity spectrum that becomes steeper with an increasing range of temperatures present. This translates to a shorter wavelength CF position for more anisothermal surfaces [*Bandfield et al.*, 2011b]. The degree of anisothermality due to surface roughness is dependent on solar incidence angle, as morning and evening sun angles create sunlit and shaded slopes with greatly differing temperatures [*Bandfield et al.*, 2011a]. The effect becomes negligible at local noon as opposing slopes approach the same temperature. The magnitude of shifts to the CF position due to anisothermality can be up to 0.4μm at high solar incidence angles, but is typically <0.1μm with observations close to noon. This effect is common as it can occur at a small scale due to surface roughness on the order of millimeters, the scale where the lunar regolith can be thermally isolated.

The binned CF value image for each crater was masked due to anisothermality effects in regions with sharp temperature transitions. The mask was created by taking the derivative of channel 4 radiance with respect to lateral distance and discarding data with values greater or less than 2 standard deviations from its mean. Regions where radiance values are transitioning between extremes - such as the interface

between a central peak and the crater floor - were discarded by the mask [Fig. 2]. The range of temperatures within a single pixel is much greater in these topographic interfaces, so when a single surface temperature is assumed there is a significant shift in the CF value, greatly affecting mineralogical interpretation [*Bandfield et al.*, 2011a].

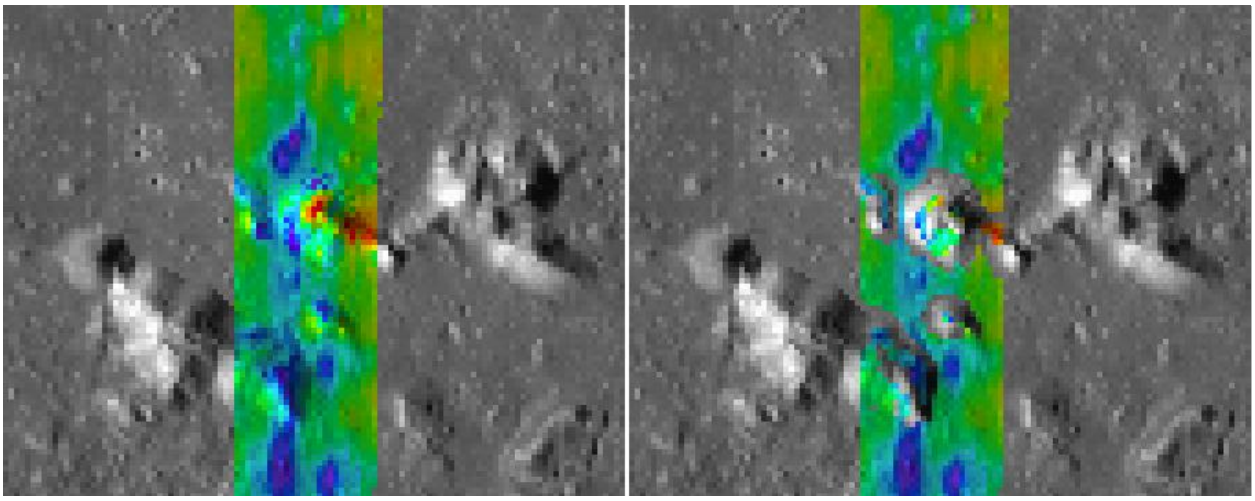

Figure 2 Example of the data mask used to discard Diviner CF data that is likely to be dominated by the effects of anisothermality, particularly on topographic boundaries where severe temperature changes occur at scales much smaller than Diviner's footprint.
Left: CF before mask ; Right: CF after mask
Colorized CF value (8.0 μm – 8.3 μm stretch) from two Diviner orbits over WAC mosaic. Close-up of the central peaks of Copernicus. Note the high CF value feature in red on the center-most peak.

2.3.2 Insolation effect

An additional effect on spectral emissivity has been found in this study that appears to be largely dependent on solar insolation and local time. The physical processes responsible for this effect have not been fully characterized, but its influence on the CF position can be quantified with inspection of the data at various slopes and local times. The apparent temperature dependence of this effect shifts the CF position in the opposite direction of the CF position shift due to anisothermality (where CF generally increases with increasing surface temperature and decreasing solar incidence angle). The behavior of this effect is complex, as it is likely a combination of multiple processes that vary as a function of local incidence angle, surface and subsurface temperatures, and topographic slope.

The magnitude of this effect is asymmetrical about local noon, which suggests that this effect is dependent on the subsurface thermal gradient that varies in intensity throughout the day. It has been shown previously that thermal gradients within the regolith of bodies in vacuum environments have an effect on mid-IR spectral features [*Cooper et al.*, 2002; *Henderson and Jakosky*, 1994, 1997; *Salisbury et al.*, 1973], but there are additional factors such as heating from nearby surfaces that have not yet been quantified. Opposite slopes of a topographic high (e.g. a central peak) experience differing amounts of integrated solar insolation throughout the lunar day, so in future efforts to model this effect it is important to note both the solar incidence angle on a surface at the time of observation as well as the elapsed time that surface has been heated.

The effect on CF position is most prominent prior to noon local time, where low temperature pixels on shaded slopes are associated with relatively high CF values, and high temperature pixels on sunlit slopes are associated with relatively low CF positions [Fig. 3, 11am]. With local times after noon [Fig. 3, 1pm], the effect is apparent for the lower temperature pixels up to ~383 K, while the higher temperature pixels (>385K) behaved as expected based on CF position shifts due to anisothermality alone with a higher CF position with higher surface temperature.

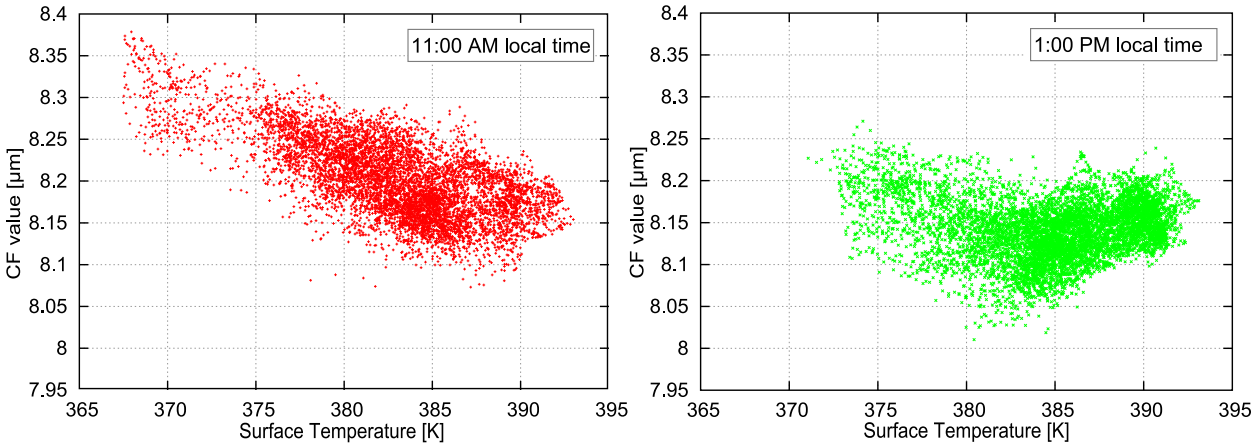

Figure 3 Scatter plot of CF value vs. surface temperature. Diviner data collected before (red) and after (green) local noon over the same location in the highlands with negligible compositional variation. The dominant effect for the pre-noon data (red) is a shift of CF values to shorter wavelengths with increasing temperature. The shift in CF value to longer wavelengths with higher temperatures is due to anisothermality - seen in the higher temperatures in the post-noon data (green).

This effect consistently causes shifts in CF position on opposite sides of a topographic slope as well as opposing crater walls. It is seen most prominently within single orbit tracks with fixed local time on north and south facing slopes. Observing the effect between east and west facing slopes is more difficult simply because it typically requires two separate orbit tracks to provide data coverage on laterally opposing slopes. CF value can vary by ~0.2 μm due to this effect with data collected prior to local noon. In order to avoid sampling CF data where this error occurs, central peak sample regions were limited to areas of relatively constant temperature that do not extend beyond a single topographic facet at Diviner's spatial resolution.

2.3.3 Space Weathering

The surface of the moon is constantly bombarded by micrometeorites, solar wind, and cosmic rays. These processes alter the optical properties of the soil by coating nanophase iron on grain surfaces as well as forming agglutinates (glassy aggregates) [*Noble et al.*, 2001; *Taylor et al.*, 2001]. Both of these forms of weathering cause a darkening of the soil at visible wavelengths, and nanophase iron implantation produces a red spectral slope into the NIR [*Le Mouélic et al.*, 2000].

The degree of maturity of lunar soil can be derived from Clementine UVVIS maps using the optical maturity parameter (OMAT) algorithm developed by *Lucey et al.* [2000]. These maps show that central peaks and crater walls are generally less weathered than the surrounding area. Mass wasting is common on the relatively steep slopes of central peaks and crater walls, exposing fresh, unweathered material.

The alteration of optical properties has shown to shift the CF position as well [*Glotch et al.*, 2012; *Lucey et al.*, 2010]. The magnitude of this shift can be determined by analyzing the CF positions associated with the Reiner Gamma albedo feature in the Procellarum basin, thought to be shielded from solar wind bombardment by a local magnetic field. The Reiner Gamma feature shows variations in OMAT values without other effects (e.g. topography), allowing for the isolation of the weathering effect on CF position. The degree of weathering was provided by the Clementine NIR OMAT parameter. Although a correction

was not applied to the data used in this study, the magnitude of the effect on CF position has been documented. An increase of 0.15 in the maturity parameter (that increases with less weathered, younger soils; ~4% change in albedo) corresponds with a decrease in CF value of ~0.1μm.

2.4 Supporting Data

The CF value data were compared against NIR spectroscopy data products to ensure that shifts in CF value are correlated with compositionally distinct features rather than temperature-dependent anomalies. For craters with average central peak CF values indicative of ultramafic compositions, hyperspectral NIR imagery was utilized to distinguish between the presence of olivine and pyroxene, as both of these minerals have moderately long CF positions. Crust thickness maps allowed for a correlation of central peak CF values with crustal composition at various depths.

The average central peak CF values were supplemented with iron abundance and optical maturity (OMAT) data from the sampled region. These maps were derived from Clementine spectral reflectance data [*Lawrence et al.,* 2002; *Lucey et al.,* 2000], and the LROC WAC global mosaic and LOLA topography provided spatial context for the Diviner CF measurements.

Central peaks with CF positions indicative of very mafic compositions were further explored using hyperspectral NIR imagery from the Moon Mineralogy Mapper (M^3) onboard Chandrayaan-1 spacecraft [*Pieters et al.,* 2009]. The M^3 instrument has 86 spectral channels between 0.42-3.0 μm with delta-wavelength of 0.04μm. The RDR data used in this study (available from PDS) was limited to global measurement mode with a spatial resolution of ~140m/pixel.

Level 1B radiance data from M^3 was converted to I/F [*Besse et al.*, 2011] with the solar spectrum provided in the PDS. The continuum slope between the 0.66μm and 1.938μm bands was removed with a simple linear correction for better interpretability of 1-2μm spectral features.

M^3 spectra from central peaks with CF features of interest were directly compared to laboratory spectra of olivine and pyroxene [*Bishop et al.*, 1995; *Mustard and Pieters*, 1989], but another method was needed to better visualize the distribution of mafic minerals. An olivine index map developed for this study is based on the integrated band depth (IBD) of olivine and pyroxene absorption features:

A typical olivine spectrum is characterized by a broad composite absorption feature centered around 1.05μm followed by a relatively flat spectrum around 2μm, while a typical pyroxene spectrum has two strong absorption features centered around 1 and 2μm [Fig. 4]. A ratio of the 1μm feature IBD with the 2 μm feature IBD sharply distinguishes the presence of olivine from pyroxene and is the value used for our olivine index maps. The method developed to create the index image is shown in Figure 4, where first the continuum line bounding the absorption band for each feature is approximated by finding the maximum reflectance value within a small range of wavelengths on both ends of the feature. The difference between measured reflectance and the continuum reflectance is summed across all bands inside the absorption feature, and the 1 μm IBD map is divided by the 2 μm map to highlight regions with strong olivine spectral signatures.

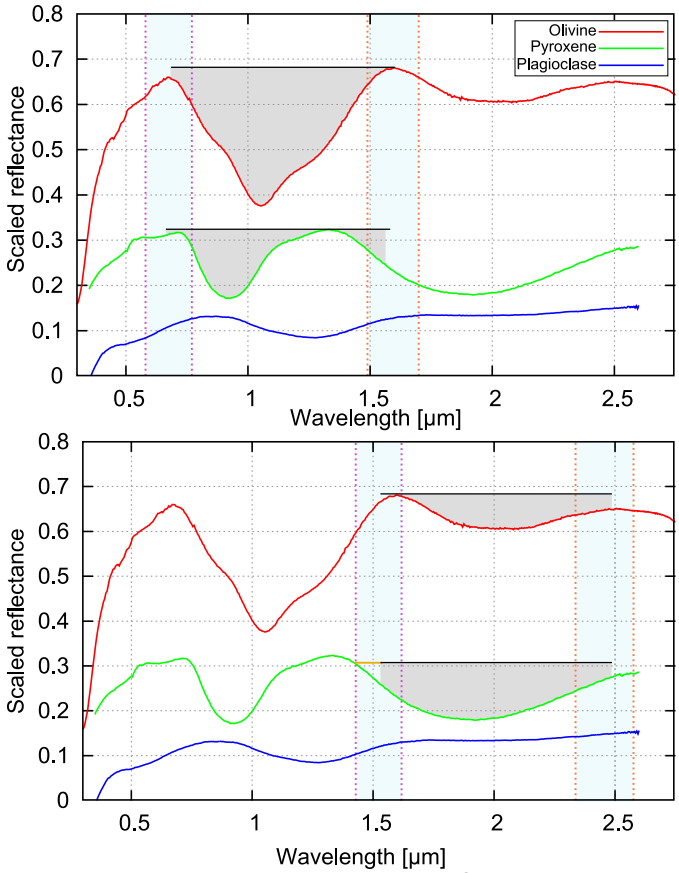

Figure 4 Creating olivine index maps from M^3 NIR hyperspectral data.
Top - Integrated band depth of the 1 μm absorption feature. Bottom - Integrated band depth of the 2 μm absorption feature.
Dashed vertical lines show the range of wavelengths that are searched for a reflectance maximum from which the band depths are calculated. NIR laboratory spectra of olivine, pyroxene, and plagioclase separates from lunar samples [*Bishop et al.*, 1995; *Mustard and Pieters*, 1989].

Band-independent noise in the form of vertical streaks is prevalent in M^3 band ratio maps so a frequency domain filter was applied to the olivine index map to improve image quality. The single pixel wide near-vertical noise can be isolated and removed with a horizontal notch reject filter applied in the frequency domain. This destriping method does not improve spectral quality (all 85 bands destriped), but it does improve image quality and interpretability in band ratio images.

Central peak CF values were also compared with 1 ppd resolution crustal thickness data presented in *Wieczorek et al.* [2006]. The data used in this study, Model 2, is a single-layer crustal thickness model with minimum crustal thickness of almost 0 km beneath the Apollo basin and a maximum thickness of about 104 km.

The depth of origin for uplifted central peak material is a function of crater diameter as described by *Cintala and Grieve* [1998], where the minimum depth of origin is coincident with the maximum depth of melting. Given a crater diameter D in kilometers, the depth of origin is $0.109D^{1.08}$. As shown in *Cahill et al.* [2009], the proximity of the central peak's depth of origin (D_{cp}) to the crust-mantle boundary (T, crustal thickness) in kilometers is T - D_{cp}. Expressed in terms of percentage of the total crustal column, (T - D_{cp}) / T is the proportion of crustal material that is at a greater depth than the depth of origin.

2.5 Crater Selection and Processing

A list of complex craters within 30 degrees latitude of the equator was compiled based on the Gazetteer of Planetary Nomenclature maintained by the USGS Astrogeology Science Center [http://planetarynames.wr.usgs.gov]. 22 complex craters that were not listed in the Catalog were also identified using the Lunar Reconnaissance Orbiter Camera Wide Angle Camera (LROC WAC) Equatorial Mosaic and included in this study [*Robinson et al.*, 2010]. Criteria used to pick the craters for this analysis are: a) easily identifiable and unambiguous central peaks resolvable at Diviner resolution, and b) Diviner data coverage over the one of more of the crater central peaks, and c) Diviner data acquired within 2 hours of noon local time to minimize CF value shifts that are a function of solar incidence angle.

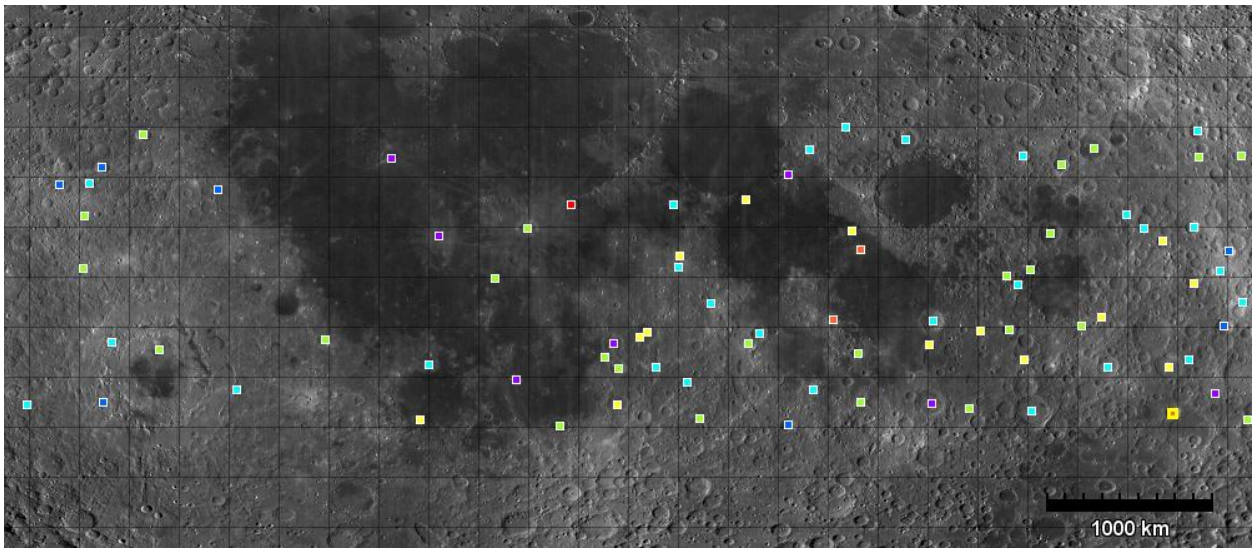

Figure 5 Location of the 135 craters examined in this study on a LROC WAC basemap from -60°:60° latitude. Gridlines every 10°.

From the 268 craters initially examined, craters with data that were clearly dominated by non-compositional shifts to the CF position within their central peaks (identified by the distinctive CF shifts over topographic features) were discarded from the survey. For the remaining 135 craters [Fig. 5], data from the central peaks were isolated from the rest of the image with a polygon mask that was drawn for each crater. Regions with highly variable topography were avoided, so the masks generally represent the CF values from one side of the central peak (e.g. the west-facing side). Because topographic features degrade over time due to regolith formation, the oldest craters in this survey typically had a larger area that we were able to sample from the central peak [Fig. 6] than newer craters with sharp peaks and valleys (e.g. Copernicus).

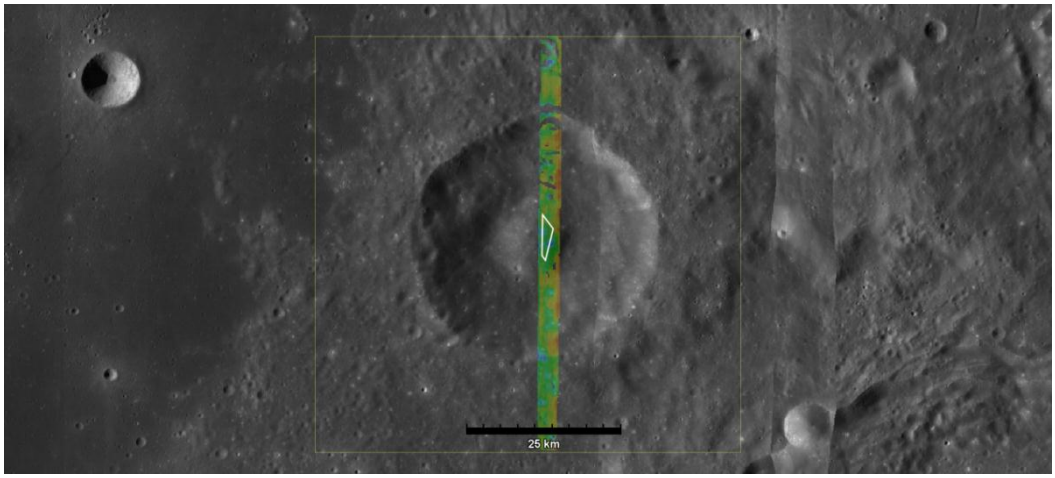

Figure 6 An example of a degraded crater (Alpetragius) with smoothed topographic boundaries. Overlain on the LROC WAC basemap is the colorized CF value image (stretched from 8.0 - 8.3 µm) with a white polygon around the region sampled for average CF value for this crater's central peak.

Data within the polygon mask were averaged to determine mean CF value of each crater's central peak as well as local crustal thickness and Clementine-derived FeO abundance, degree of maturity (OMAT), and 750nm reflectance. Inner crater walls were also examined for any signs of mafic exposures, although the data quality is much worse on the highly variable terraced crater walls so only one acceptable feature was located.

The random error associated with the Diviner CF value was approximated using data from a relatively flat, featureless surface at local times ranging between 1000 and 1400. The sampled region is in the

nearside mare centered around -54° E, 0.26° N where there are no craters greater than 1 km in diameter. The data were processed in the same manner as described above, including the radiance derivative mask that removed much of the data overlapping with small craters. A uniform region of ~1100 to 1600 pixels within a single orbit track was selected for each local time. Although the sampled regions for each local time do not directly overlap due to limitations in coverage, Clementine-derived FeO and maturity maps show compositional uniformity within the sampled regions such that the only variations in CF value are due to local time and random error. The mean and standard deviation CF values are plotted versus local time in Figure 7.

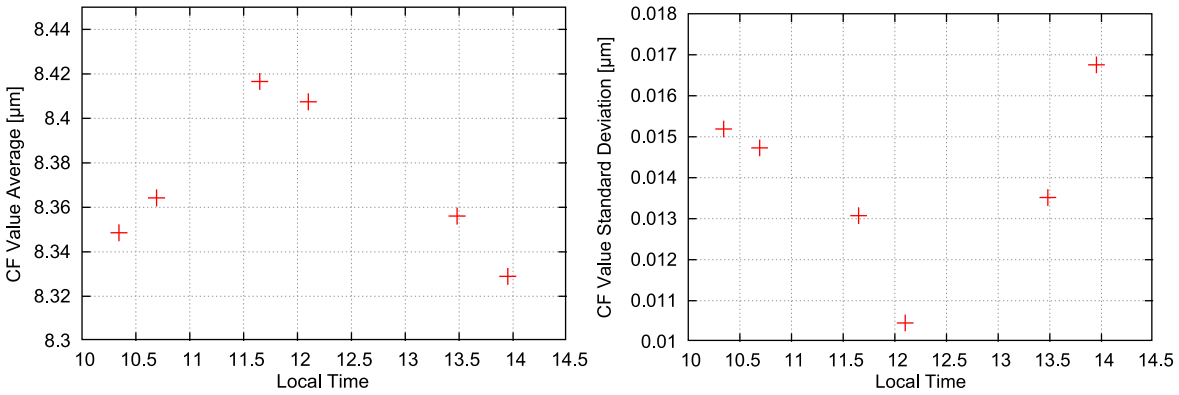

Figure 7 Random error in Diviner CF value. Left - Average CF value vs. Local time. Right - Standard deviation of CF value vs. Local time.

3 Results

3.1 Distribution of Central Peak Compositions

Based on our survey of central peak composition for 135 craters within 30° latitude of the equator [Table 2, Appendix], 52.6% of craters have a central peak CF value below 8.10 µm, which is indicative of predominantly plagioclase-rich compositions. Out of the 52.6%, 87.3% of these were craters in the highlands. The mean CF value for all craters is 8.10 µm with a maximum of 8.48 µm (Eratosthenes crater) and a minimum of 7.70 µm (Aristarchus crater). Note that the sample size for highlands craters makes up a much larger proportion of the all craters sampled (105 out of 135) than craters in the mare (30 out of 135), so the compositional distribution of mare craters may not be as representative of the population as that of highlands craters that were analyzed.

Central peak CF values were binned from 7.6 µm - 8.56 µm at increments of 0.04 µm to produce a histogram [Fig. 8a]. The distribution is bimodal with peaks at 8.08 µm and 8.16 µm. The 8.08µm peak (CF values between 8.04 µm - 8.08 µm) is made up of ~19.3% of the surveyed craters, 21.0% of the highlands craters, and 13.3% of the mare craters. The longer wavelength 8.16 µm peak holds 16.3% of all craters, representing 15.2% of the highlands craters and 20.0% of the mare craters. Based on the global CF value histogram from *Greenhagen et al.* [2010] [Fig. 8b], the variety and range of central peak silicate compositions is similar to those found globally on the surface of the Moon.

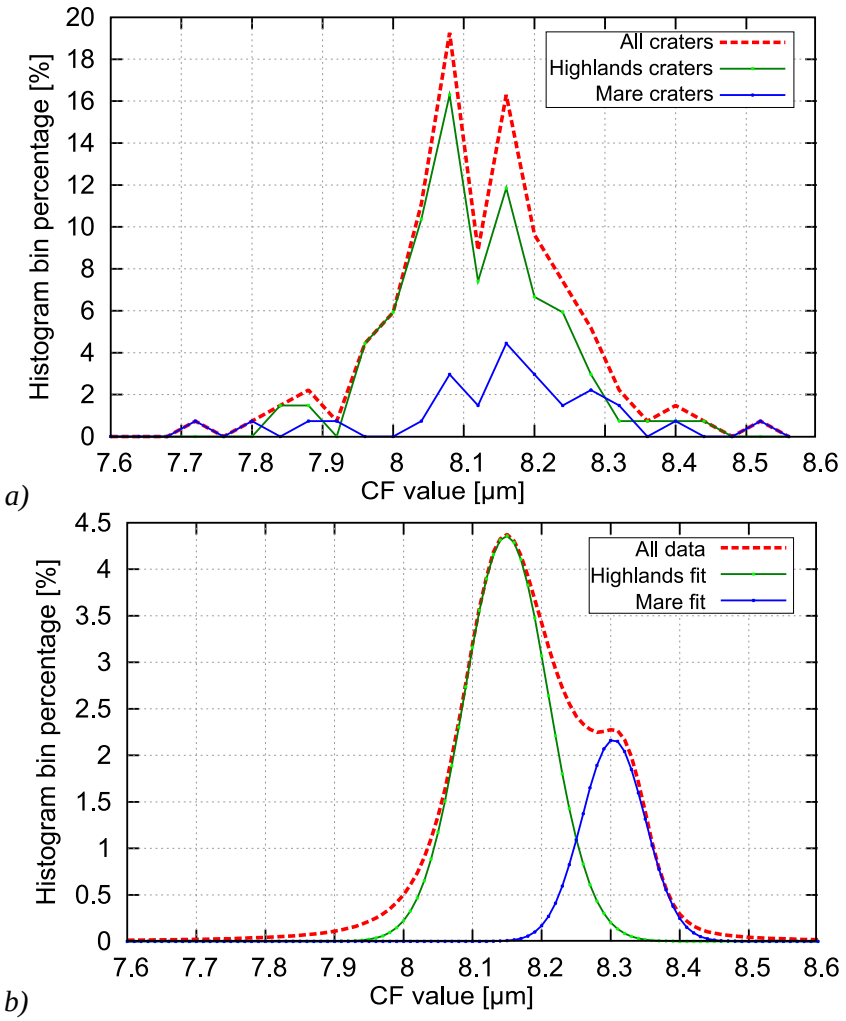

Figure 8 CF value distributions for crater central peaks from this study [a, top] and a global compositional study of CF values from Greenhagen et al. [2010] [b, bottom]. The central peak histogram [a] shows the distribution of CF values for all 135 craters (dashed line). CF values are binned in 0.04 µm increments from 7.6 µm – 8.56 µm. The distribution is bimodal, with maxima at CF values of 8.08 µm and 8.16 µm. The global histogram [b] also shows a bimodal distribution (dashed line) with the modal mean of highlands terrain at 8.15 µm and mare terrain at 8.3 µm.

The CF value of crater central peaks is not strongly correlated with local crustal thickness, central peak depth of origin, or depth of origin relative to the crust-mantle boundary [Fig. 9]. Mean crustal thickness for craters in the highlands is 50.2 km and 44.5 km for mare craters. Humboldt crater (199.5 km diameter) has multiple central peaks that are composed of uplifted material from the lower crust, only ~2 km from the crust-mantle interface. However, the composition of the Humboldt crater central peak shows little evidence of mantle-like mafic material and is largely anorthositic, with an average CF value of 8.08 µm.

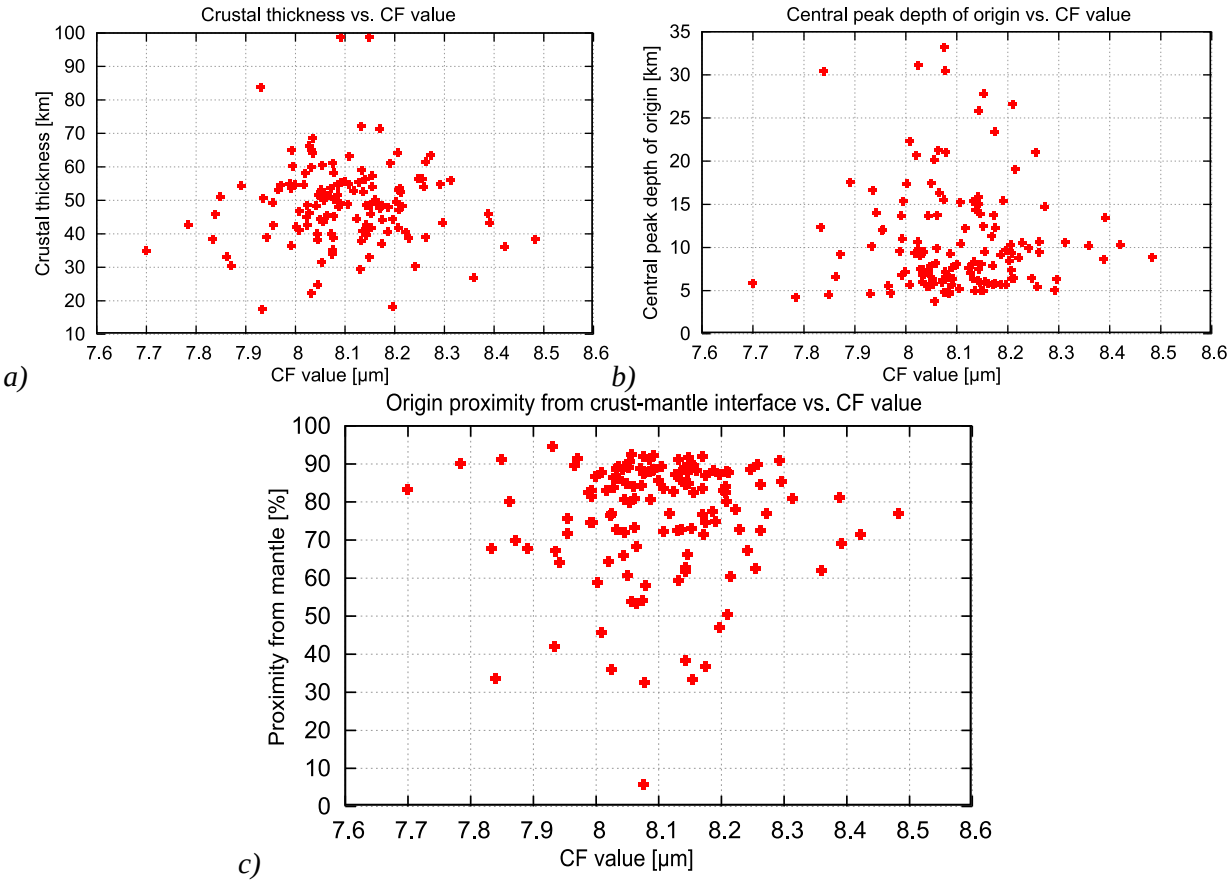

Figure 9 Comparison of central peak CF values with crustal depth.

Central peak CF values appear to be correlated with Clementine-derived FeO abundance and OMAT values [Fig. 10]. Longer-wavelength CF values, indicative of high proportions of mafics relative to plagioclase, correspond to higher abundance of FeO [Fig. 10a]. Craters with central peaks that are more optically weathered (low OMAT value) show higher CF values than less weathered central peaks [Fig. 10b], and the correlation is strongly linked to surface albedo [Fig. 10c].

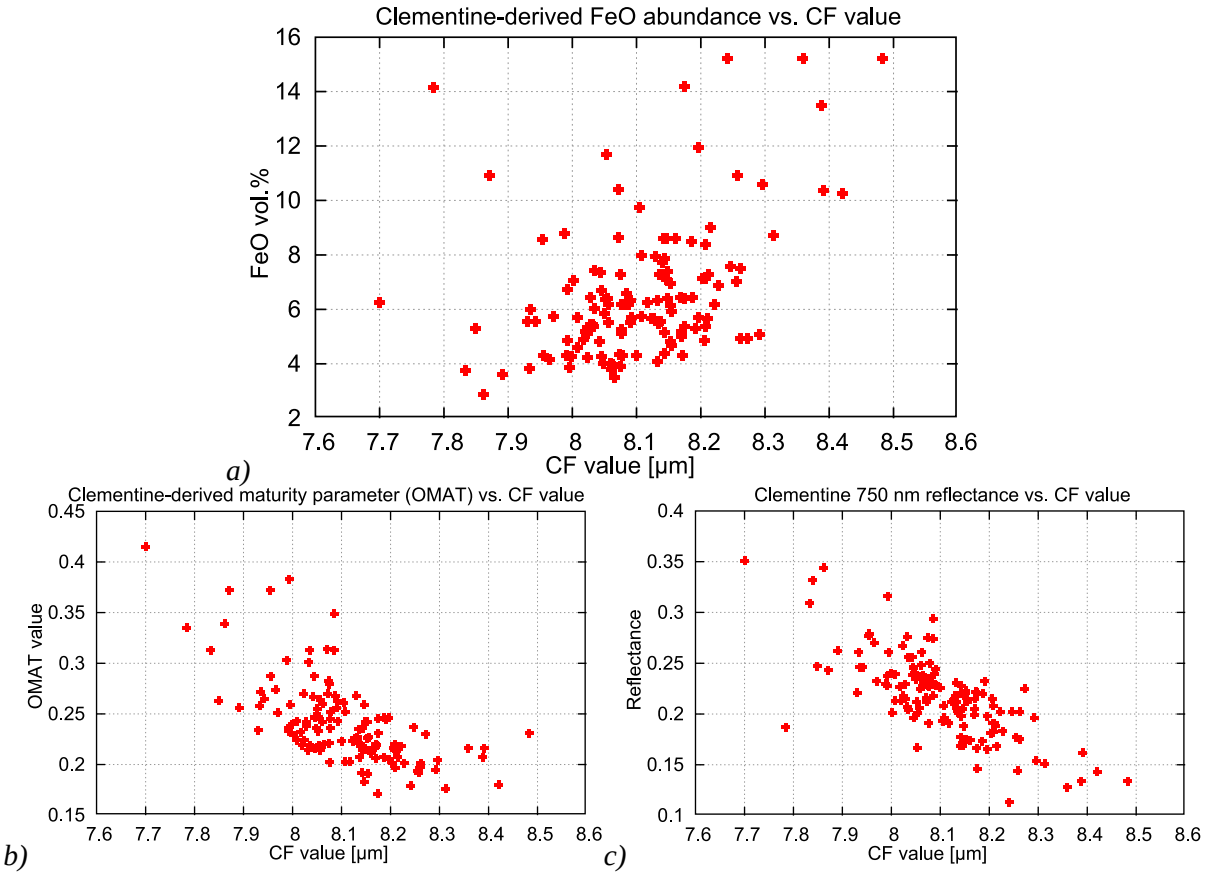

Figure 10 Clementine-derived FeO abundance [a], OMAT maturity parameter [b], and 750nm reflectance [c] vs. CF value.

Only 6 craters (4.4%) were found with CF values above the average global mare CF value of 8.3µm [*Greenhagen et al.*, 2010] - Eratosthenes, Taruntius, Gutenberg craters within the nearside mare and Plummer, Scaliger, and Barringer craters in the farside highlands but near basin rims. Although many of the more felsic CF values were found in highlands craters, the two lowest CF values were located on the nearside mare in the central peaks of Aristarchus and Kepler craters. Both of these craters are in Procellarum basin where the crust can be more than 10 km thinner than in the highlands, so these craters must be located near local sources of highly felsic crustal material.

3.2 Regional Central Peak Compositions

3.2.1 Mare Crater Compositions

Craters within the mare show a wide range of compositions in their central peaks [Fig. 8a]. The crater with the most mafic central peak and the crater with the most felsic central peak are both found in the nearside maria. 30% of the mare craters have central peak CF values below 8.1 µm, and 60% have central peak CF values between 8.1 µm and 8.3 µm. The modal mean CF value for mare craters, based on the 0.04 µm bin histogram, is 8.16 µm.

The central peak with the most mafic CF value is in the ~59 km diameter Eratosthenes crater (348°E, 14.5°N) along the southern rim of Imbrium basin. The average CF value of the mafic exposure in the central peak is 8.48, which between the CF positions of the pyroxene endmember (8.25 µm) and the olivine/forsterite endmember (8.67 µm) [Table 1], suggesting an olivine-rich composition with a small proportion of pyroxene or a very small proportion of plagioclase. The feature is on the right leg of the central peak [Fig. 11] along a relatively constant slope with no dramatic topographic changes.

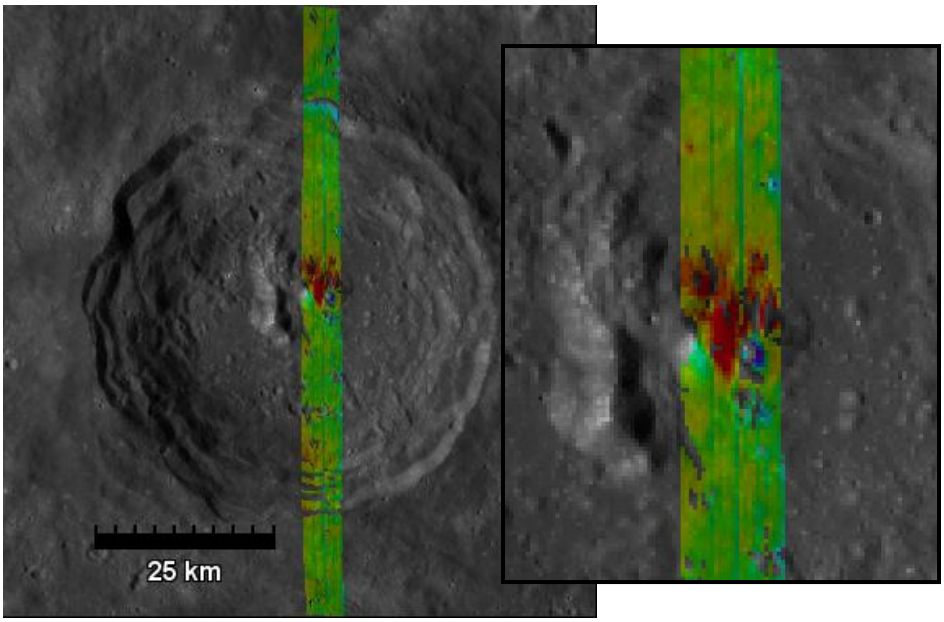

Figure 11 Eratosthenes crater, two orbits of data shown as colorized CF value (8.0-8.4 µm stretch) over LROC WAC basemap. Close-up of central peak on the right.

Average Clementine derived FeO abundance in this feature is 15.2 vol.% and average OMAT value is 0.23 (close to average central peak maturity, 0.24). The crust is ~39 km thick in this location and the estimated depth of origin for peak material is ~9 km below the surface - far from the crust-mantle boundary. Assuming that the thickness of the mare basalt lens is less than 9 km, the central peak of Eratosthenes could be uplifting some of the original crust that covered the nearside surface prior to basin formation.

Another mafic crater in the mare is Taruntius, a 57 km diameter crater on the northwest rim of Mare Fecunditatis (just east of Mare Tranquillitatis and south of Crisium at 46.5°E, 5.5°N). The CF value in its peak is 8.39 µm, so its proportion of mafics to plagioclase is slightly higher than that of typical mare basalt. Average FeO abundance is 13.5 vol.%, and OMAT is 0.21 (slightly more weathered than average central peaks). Crustal thickness at this location is 46 km with an estimated central peak depth of origin of ~8.6 km.

Aristarchus crater in the center of Procellarum basin has shown evidence of silicic magmatism exposed in its crater rays [*Glotch et al.*, 2010]. The central peak appears to be extremely silicic as well, with a concave-up 3-point Diviner spectrum that prevents usage of the parabolic interpolation method to derive the CF value. Based on the results of *Glotch et al.* [2010] we approximate the upper limit of the central peak CF value to be ~7.70 µm. Clementine-derived FeO abundance of 6.3 vol. % at the central peak is about half that of typical mare basalt.

Kepler crater, also in Procellarum basin ~20° to the south of Aristarchus crater, shows a central peak CF value of 7.78 µm. This composition is also very felsic but is likely a mixture with small amounts of mafic components, as the CF value was resolvable using the 3-point Diviner spectrum. The sampled region contains about 14.1 vol. % FeO, which similar to the surrounding mare basalt. Kepler crater is relatively small (29.5 km diameter), so the material in its central peak originated from only ~4 km into the crust - potentially near the boundary between the mare basalt lens and the original anorthositic crust.

Copernicus is a 96 km diameter crater in Insularum basin with central peaks originating from ~15 km below the surface into a ~40 km thick crust. This is the only crater found in this study that shows unambiguous evidence of a mafic exposure in its crater walls [Fig. 12]. Its center-most peak shows a relatively felsic average CF value of 8.14 µm, while the crater wall feature shows a more mafic CF value of 8.33 µm. The center-most peak OMAT is 0.31, indicating a relatively young surface exposure that could partially account for the unusually low central peak CF value. The wall feature is closer to average central peak optical maturity with an OMAT of 0.24. Clementine-derived FeO abundance is a relatively low 6.7 vol.% in the center-most peak, while the wall feature has ~10.1 vol.% FeO.

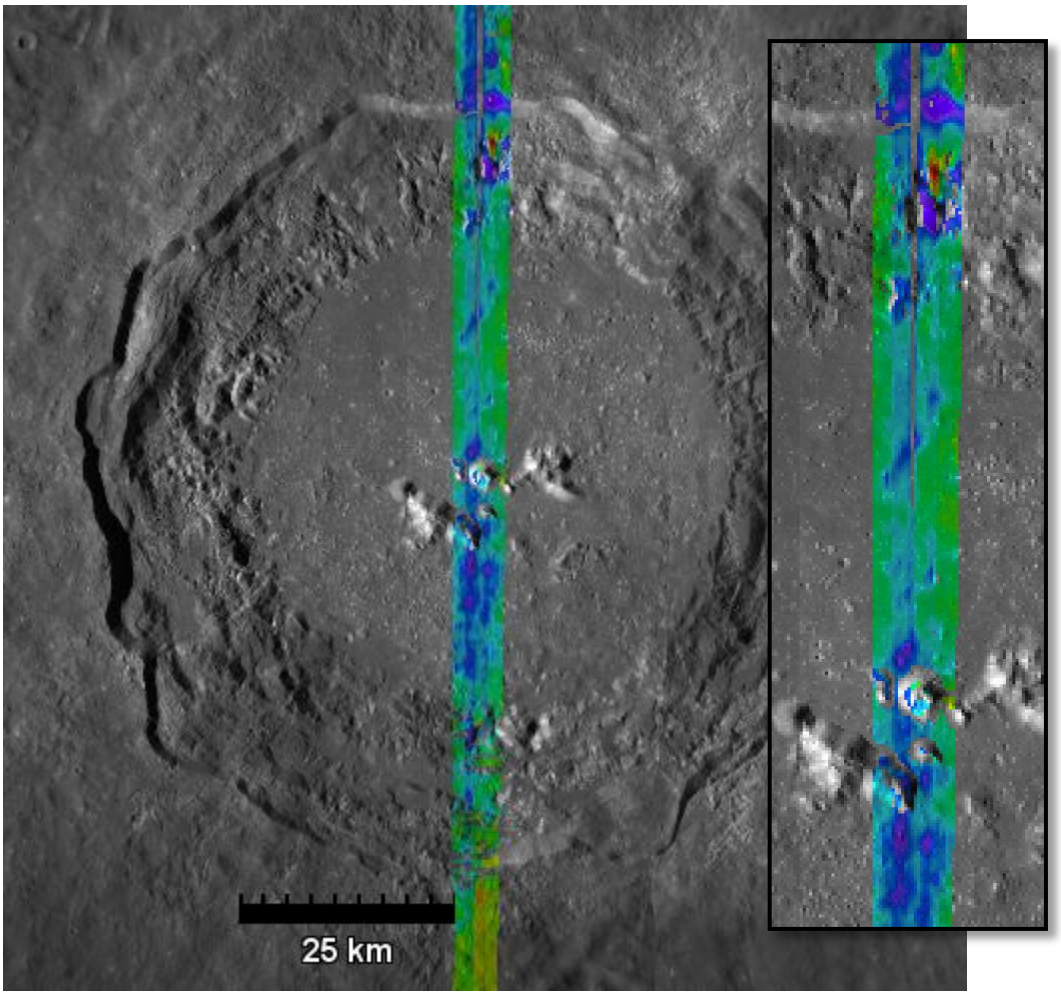

Figure 12Copernicus crater. Two orbits of data shown as colorized CF value (8.0-8.4 µm stretch) over LROC WAC basemap.

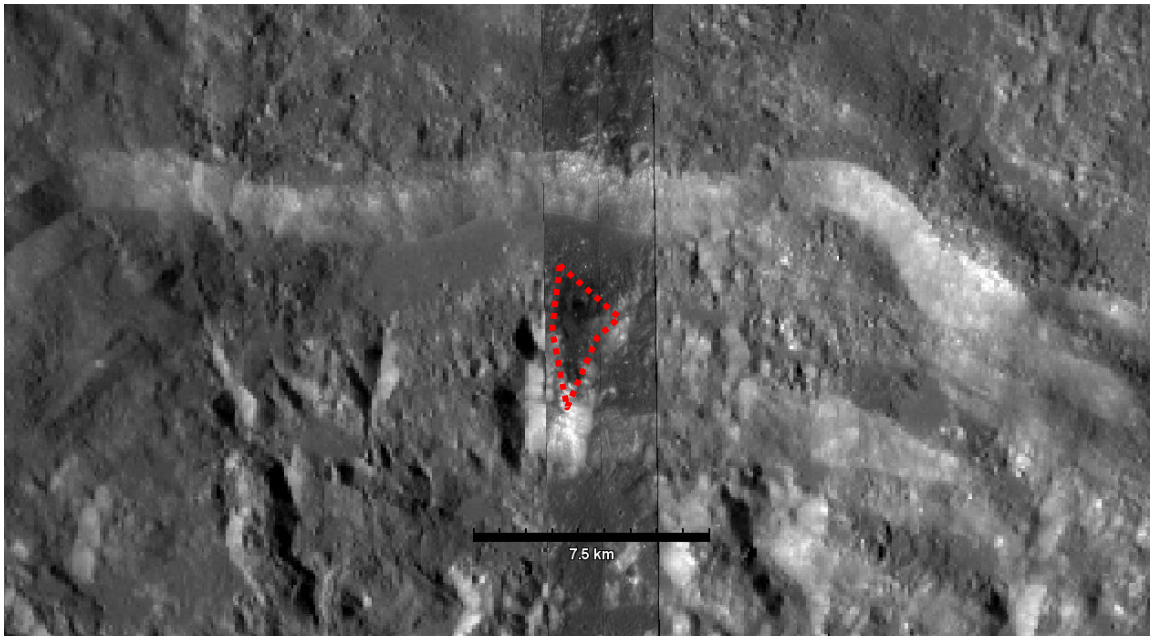

Figure 13 LROC NAC image (M127063668R) over the northern wall CF feature. Dotted red shape shows approximate boundary of CF feature.

The wall feature is approximately 2.5 km long and 0.9 km wide and located just below the top of the first terrace from the northern crater rim. The shape and breadth of the wall feature strongly suggests that the CF value of the feature is representative of a compositional variation rather than a temperature-dependent shift. High resolution LROC NAC imagery (M127063668R) shows an unusually dark region that coincides with the mafic crater wall CF feature [Fig. 13]. The area appears to be overlapping or surrounded by several small craters or pits.

3.2.2 Highlands Crater Compositions

Highlands crater central peaks show a wide range of compositions much like the mare craters. 55% of the highlands craters have central peak CF values between 7.9 μm and 8.1 μm, so most highlands craters show central peak compositions with mafics/plagioclase ratios similar to that of the anorthositic highlands. 38% of the highlands craters have CF values between 8.1 μm and 8.3 μm, implying that many of the highlands craters are uplifting material with mafics/plagioclase ratios similar to that of mare basalt.

Plummer and Barringer craters near the northern rim of South Pole-Aitken basin are two of the three highlands craters with ultramafic compositions. The average CF value of the central peak of Plummer crater is 8.42 μm, and for Barringer crater is 8.36 μm. The central peak Clementine-derived FeO abundance is 10.3 vol.% for Plummer crater. Barringer crater contains about 5 vol.% more FeO in its central peak than Plummer crater, despite its lower CF value. Due to their proximity to South Pole-Aitken basin the crustal thickness is relatively low for these craters, with Plummer crater uplifting material from ~26 km depth with a 31 km thick crust, and Barringer crater uplifting from ~17 km into the 27 km thick crust.

Olcott crater (20.4° N, 117.5° E) is a 80 km diameter crater with the most felsic central peak in the highlands, with a CF value of 7.83 μm. The central peak is less weathered than the average central peak with an OMAT value of 0.31, and shows a very low FeO abundance of 3.73 vol.%. Crustal thickness is relatively low where Olcott is located (38 km), and the material being uplifted in its central peak is from ~12 km depth, above ~68% of the crustal column.

4 Discussion

4.1 Global

4.1.1 Histogram

The histogram of CF values from our central peak survey shows two maxima at CF values of 8.08 and 8.16μm that represent the most frequently occurring peak compositions [Fig. 8a]. The highland and mare crater distributions are skewed towards their respective maxima but are not distinctly split into two populations. The global CF distribution from Greenhagen et al shows the modal mean CF values for the mare (8.3μm) and highlands (8.15μm) terrains. The maxima in the central peak CF distribution occur at shorter wavelengths than the global CF distribution, which can be partially attributed to the fact that

central peaks tend to be less optically mature than surrounding terrain, shifting the CF position shortward up to ~0.1μm.

The similarity between the global CF distribution from Greenhagen et al and our central peak CF distribution implies that uplifted material found in the central peaks is not significantly different from the range of compositions found on the lunar surface. This does not imply that crustal composition is uniform with depth, however, as many craters in the highlands have central peaks that have a similar mafics/plagioclase ratio to mare basalt, and some of very felsic central peaks with the lowest CF values are located in the maria.

There is a prominent dip between the maxima in the central peaks histogram, suggesting that intermediate compositions between highlands and mare-like rocks occur less frequently in central peaks. About 36% of highlands craters and 57% of mare craters have central peaks with CF values between 8.15μm and 8.3μm, indicating that a significant portion of the central peak material has mafic compositions with similar mafics/plagioclase ratios as mare basalts, regardless of surface terrain. Apollo samples of mare basalts typically contain 20-40% plagioclase [*BVSP*, 1981], which to first order is consistent with a CF position between ~8.15 - 8.4 μm (without compensating for optical maturity effects).

4.1.2 CF Values Compared to FeO, OMAT

CF value appears to be strongly correlated with Clementine-derived FeO abundance and optical maturity. Note that there are 4 craters in this survey that lacked Clementine 950nm band data coverage so they are not included in this analysis (Langrenus, Petavius, Crater 24 and 33).

CF value increases with increasing FeO vol.% [Fig. 10a], although Kepler crater in the Procellarum Basin is a notable outlier with an average central peak CF value of 7.78 μm and 14.1 vol.% FeO (2nd lowest CF value and 3rd highest FeO abundance). Rock compositions with less than 4 vol.% FeO are difficult to form on the Moon, resulting in a 4% cut-off in the vertical axis. 75% of the central peaks have an FeO

abundance between 4 - 8 vol.%, where the CF value ranges between 7.85 μm and 8.29 μm (excluding Aristarchus crater, where the CF value is approximate).

CF value vs. optical maturity parameter (OMAT) shows a negative trend [Fig. 10b] – CF value decreases as OMAT increases (i.e. CF position increases with more mature surfaces). The CF value appears to vary freely with older surfaces (lower OMAT value), ranging between 8.0-8.5μm for surfaces older than the mean OMAT value for this data set (0.24). CF value becomes more constrained with younger surfaces, decreasing linearly with increasing OMAT values.

4.1.3 CF Values Compared to Crustal Depth

CF value is not correlated with the depth of origin of the peak material [Fig. 9b]. Central peak composition appears to be independent of the crust thickness [Fig. 9a], peak depth of origin [Fig. 9b], and the proximity of that depth of origin to the crust-mantle boundary [Fig. 9c]. This implies that craters that are theoretically uplifting deeply sourced crustal material do not have central peak compositions significantly more mafic than those that are uplifting material closer to the surface. Although a wide range of central peak compositions have been found, their depths of origin relative to the crust-mantle boundary do not show a clear felsic-to-mafic gradient that was expected.

Recent findings by *Pieters et al.* [2011] suggest alternate mechanisms that could have formed unusual lithologies within the crust that is not dependent on the depth they formed in. Mineralogical analysis of M^3 spectra by [*Pieters et al.*, 2011] revealed small (~few km), localized exposures of Mg-Al spinel alongside orthopyroxene and olivine in the inner ring of Moscoviense. They identified 5 unusually homogeneous regions of spinel, orthopyroxene, and olivine-rich compositions that are distinct from each other as well as the highly anorthositic surrounding terrain. Unlike olivine and pyroxene, spinel does not form in silica-rich magma bodies so its presence in conjunction with these mafic silicates is highly unusual. The favored formation mechanism for these regions is endogenic – the formation of Moscoviense basin could have uplifted and exposed mafic plutonic systems that had undergone fractional

crystallization. The crystallization process would initially produce layers of olivine and pyroxene, depleting the silicate reservoir within the pluton and allowing the remaining Mg and Al to form spinel.

Gross and Treiman [2011] supported these findings with a spinel-rich lunar meteorite with similar composition to the regions described by *Pieters et al.* [2011]. The clasts in the meteorite show a textural disequilibrium between the very fine-grained spinel and pyroxene, suggesting rapid cooling and low pressures during formation. This implies that the spinel-rich regions found by Pieters et al did not form deep within the crust, and the formation of non-anorthositic compositions is not necessarily dependent on the proximity of the source melt to the mafic mantle.

An additional source of evidence supporting our findings of globally distributed mare basalt-like compositions is from lunar regolith breccia meteorites, which are consolidated samples of fine-grained lunar soil that fused together during impact events. A study of these meteorites by [*Korotev et al.*, 2009]has shown that they are of intermediate compositions between feldspar (3-7% FeO) and basalt (17-23% FeO). *Joy et al.* [2010] found several meteorites that are compositionally consistent with a cryptomaria source where mare basalt intrusions failed to reach the surface.

4.1.4 CF Values Compared to NIR-Derived Composition

A comparison of central peak CF values to mineralogical abundances from *Cahill et al.* [2009] show no clear correlations between CF value and olivine, clinopyroxene, orthopyroxene, and plagioclase abundance. Only 16 craters from their study overlapped with the ones investigated here, and exact locations sampled from the central peaks may differ between the two studies, preventing direct mineralogical comparisons. Ongoing work by *Lucey and Greenhagen* [2012] is utilizing CF data in conjunction with hyperspectral data from Kaguya Spectral Profiler instrument to better constrain mineralogical abundances.

4.2 Local

Craters in this study exhibiting the lowest CF values in their central peaks (e.g. Aristarchus, Kepler) are located in the same nearside maria region as craters with some of the highest CF values (Eratosthenes, Taruntius). Aristarchus crater is located in a region covered in highly silicic compositions [*Glotch et al.*, 2010], which can account for the relatively low FeO abundance (~6.3 vol.%) and extremely low CF (<7.7 μm). Kepler crater, on the other hand, has a high FeO abundance (~14.1 vol.%) but an average CF value of 7.78μm in its central peak. This could be due to the relatively small crater diameter of Kepler (29.5 km) that is around the transition diameter between simple and complex craters, resulting in an irregular and off-center peak that likely uplifted anorthositic crust just below the mare basalt lens. The disparity between the low CF value and high FeO abundance could be explained by the contrast between the relatively unweathered central peak of Kepler combined with a FeO abundance similar to typical mare basalts, or a slight misregistration between the Clementine and Diviner data sets.

Out of the 135 craters surveyed, only 6 craters exhibit central peak compositions more mafic than average maria, with CF values greater than 8.3μm. We can infer from this that ultramafic compositions are uncommon within the lunar crust and mantle-like compositions of pure olivine are not being uplifted by complex craters. Clementine-derived FeO abundances for these 6 craters are between 9-15 vol.%.

Eratosthenes crater shows a central peak CF value of 8.48 μm, indicative of an olivine-rich composition with small amounts of pyroxene and/or plagioclase. The CF value map [Fig. 11] shows that the mafic exposure on the central peak of Eratosthenes is broad and sustained on both north and south-facing slopes, indicating that the CF position is unaffected by temperature-dependent anomalies. The olivine index image derived from M^3 spectra [Fig. 14a] shows a strong and extensive olivine feature on the eastern leg of the peak that overlaps with the high CF value feature, indicating a high abundance of olivine and relatively low abundance of pyroxene. Other prominent olivine features can be seen on a small region on the west leg of the peak as well as a large feature on the northeast outer crater wall.

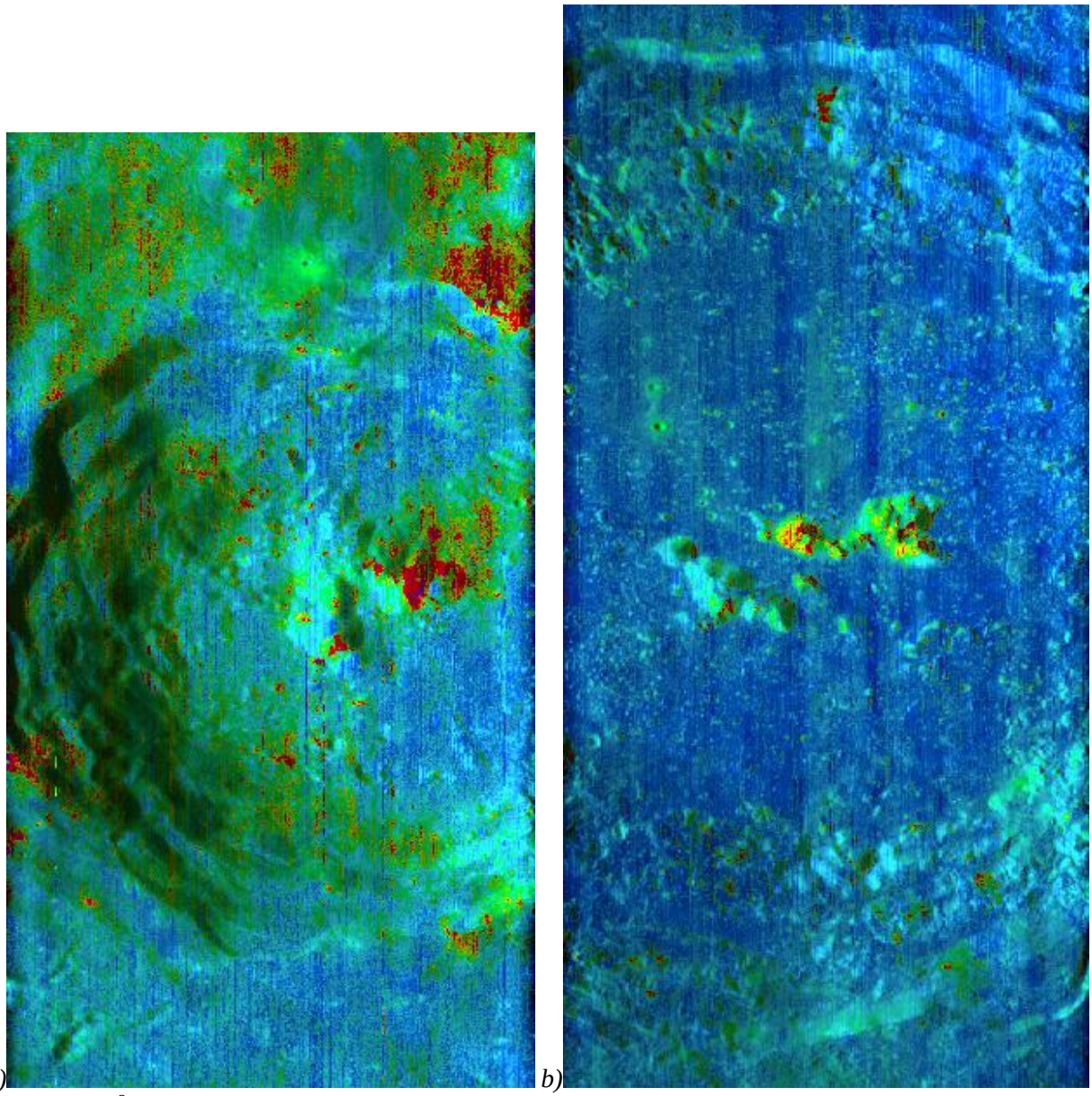

a) *b)*

Figure 14 M^3-derived olivine index maps of Eratosthenes [a] and Copernicus [b] craters. The central peak of Eratosthenes crater shows an extensive olivine feature on the eastern leg of the peak that overlaps with the high CF value feature (8.48 μm). Other prominent olivine features can be seen on a small region on the west leg of the peak as well as a large feature on the northeast outer crater wall. Copernicus crater generally shows lower olivine indices than Eratosthenes, with moderately strong olivine features on the center-most and eastern peaks. Average CF value of the center-most peak is 8.14 μm, which suggests a bulk composition rich in plagioclase with some olivine mixed in. The concentrated feature in the northern wall likely has a bulk composition with a higher proportion of olivine than the central peaks, with a corresponding CF value of 8.33 μm

Copernicus crater [Fig. 12], reported in previous works to contain nearly pure exposures of olivine in its central peaks [*Cahill et al.*, 2009; *Tompkins and Pieters*, 1999; *Yamamoto et al.*, 2010, among others], shows an average CF value of 8.14 μm at its center-most peak, consistent with an anorthosite-rich

composition with small amounts of olivine mixed in. The northern crater wall, however, shows a long exposure of more mafic material with an average CF value of 8.33μm. FeO abundance is 6.7 vol.% in the central peak and 10.1 vol.% in the northern wall feature, and both wall and peak features fall along the FeO vs. CF trend line. The northern wall feature had previously been identified as potentially olivine-bearing by *Lucey et al.* [1991] using telescopic NIR spectra. One possible source of unique crater wall compositions could be the ponds of impact melt that can be trapped on top of the terraces that are tilted outward from the center of the crater [*Melosh*, 1989]. The small craters or pits near the feature could be exposing the melt, allowing it to be distinguishable from the ubiquitous regolith.

The olivine index image based on M^3 spectra of Copernicus crater [Fig. 14b] show strong olivine features in both the central peaks and northern wall CF feature. Copernicus crater generally shows lower olivine indices than Eratosthenes, with moderately strong olivine features on the center-most and eastern peaks. The northern wall feature seen in the CF value image coincides directly with the major olivine feature in the index image, and the rest of the crater wall shows several much smaller olivine features (particularly in the southeastern wall). The center-most and eastern central peaks show extensive evidence of olivine in the index image, which is not found in the CF value imagery. This could imply small amounts of olivine mixed into a predominantly plagioclase-rich composition, resulting in a felsic bulk composition with a low CF value.

4.3 Implications

Most of the uplifted mafic material found in central peaks shows a silicate composition with a mafic component similar to mare basalt, which could be sourced from a mix of felspathic crust with mafic plutons or cryptomaria. The CF position of pyroxene falls around 8.25μm in simulated lunar conditions [*Greenhagen et al.*, 2010], so theoretically it is possible that the majority of the uplifted material (average CF of 8.1μm) is nearly pure pyroxene. However, pyroxene is a cumulate crystallized in an intermediate

environment along with olivine, so pure pyroxene rock does not exist on the Moon in such abundance and it is much more likely that these central peaks are a mix of all 3 minerals.

The wide variety of compositions found in both mare and highlands crater central peaks indicates a great deal of inhomogeneity in the lunar crust. The extensive 'plumbing' that transported mare basalt into the nearside basin could contribute to the wide range of compositions found in this study, particularly in the nearside maria. The lack of correlation between central peak CF values and crustal thickness could be primarily attributed to the Moon's complex cratering history that constantly overturned the original crust's stratigraphy. A possible scenario is that the impacts included in this study have uplifted previously overturned stratigraphy, so the stratigraphic sequence exposed in central peaks may be incoherently inverted. The outlier craters in the survey that have central peaks with very low or very high CF values may be examples of regional crustal variation (e.g. plutonic systems), whereas the bulk of the craters show a more homogenized crust due to previous impact events.

A recent hypothesis from *Jutzi and Asphaug* [2011] suggests that the farside highlands are an accretionary pile from a small companion moon colliding into the far side of the Moon at relatively low velocity (2-3 km/s). The companion moon evolved more quickly than the Moon, with a crust and solid mantle but little to no core. The collision is thought to have occurred when the Moon's magma ocean had largely solidified. The modeled hemispherical thickness of the accreted layer is consistent with the dimensions of the farside highlands. This is a possible cause for the wide variety of compositions found uplifted in highlands craters with no correlation to the peak's depth of origin - the collision of the companion moon could have created a mixed intermediate layer between the accretionary pile and the Moon's original farside surface.

5 Conclusions

Uplifted crustal material found in the central peaks of lunar craters show a vast compositional diversity in both mare and highlands terrain. The range of compositions is comparable to that found on the surface of

the Moon, but the uplifted material is not necessarily identical compositionally to that of the surrounding terrain. It is not uncommon for a crater in the highlands to uplift material that contains a similar amount of mafic material as typical mare basalt, which could be sourced from cryptomaria or mafic plutons that occur globally. Central peak composition is not correlated with crustal thickness or the depth of origin for uplifted peak material. Copernicus crater has a relatively felsic CF value in its central peak but shows a mafic exposure in its terraced northern wall, possibly composed of impact melt that has been exposed by small recent craters. Eratosthenes crater shows the strongest evidence of an ultramafic exposure in its central peak in both the CF value and M^3-derived olivine index images.

Future work that should be conducted includes corrections for the various non-compositional CF shifts in conjunction with the development of a topographic data set of similar resolution as Diviner data. Central peak CF values should be compared to the compositional trends and CF ranges of the local terrain immediately surrounding the crater, which will allow for a more robust correlation between central peak and regional composition. Higher resolution crustal thickness maps (e.g. from Kaguya data [*Ishihara et al.*, 2009]) could improve comparisons between our bulk compositions and the depth of origin of uplifted material relative to the crust-mantle boundary.

Acknowledgements

I would like to thank Josh Bandfield and the Diviner science and operations teams at UCLA and Jet Propulsion Laboratory for their support. Jean-Pierre Williams at UCLA for developing data processing script that was vital for this project, Mark Sullivan at UCLA for technical support, and Ben Greenhagen at JPL for supplementary Diviner data. Many thanks to my Masters committee members, Alan Gillespie and Bruce Nelson, for feedback and advice.

References

Bandfield, J. L., R. R. Ghent, A. R. Vasavada, D. A. Paige, S. J. Lawrence, and M. S. Robinson (2011a), Lunar surface rock abundance and regolith fines temperatures derived from LRO Diviner Radiometer data, *Journal of Geophysical Research*, *116*, 1-18, doi:10.1029/2011JE003866.

Bandfield, J. L., P. O. Hayne, R. R. Ghent, B. T. Greenhagen, and D. A. Paige (2011b), Lunar Surface Roughness and Anisothermality Effects on Infrared Measurements, in *Lunar and Planetary Science Conference*, vol. 42, p. 2468.

Basaltic Volcanism Study Project (BVSP) (1981), *Basaltic Volcanism on the Terrestrial Planets*, Pergamon Press, Inc., New York.

Besse, S., J. M. Sunshine, M. I. Staid, and N. E. Petro (2011), Compositional variability of the Marius Hills volcanic complex from the Moon Mineralogy Mapper (M3), *Journal of Geophysical Research*, *116*, 1-15, doi:10.1029/2010JE003725.

Bishop, J. L., C. M. Pieters, R. G. Burns, and J. O. Edwards (1995), Reflectance spectroscopy of ferric sulfate-bearing montmorillonites as Mars soil analog materials, *Icarus*.

Cahill, J. T. S., P. G. Lucey, and M. A. Wieczorek (2009), Compositional variations of the lunar crust: Results from radiative transfer modeling of central peak spectra, *Journal of Geophysical Research*, *114*(E9), 1-17, doi:10.1029/2008JE003282.

Cintala, M. J., and R. A. F. Grieve (1998), Scaling impact melting and crater dimensions: Implications for the lunar cratering record, *Meteoritics & Planetary Science*, *33*(4), 889–912, doi:10.1111/j.1945-5100.1998.tb01695.x.

Colwell, J. E., and B. M. Jakosky (2002), Effects of topography on thermal infrared spectra of planetary surfaces, *Journal of Geophysical Research*, *107*(E11), 1-6, doi:10.1029/2001JE001829.

Cooper, B. L., J. W. Salisbury, R. M. Killen, and A. E. Potter (2002), Midinfrared spectral features of rocks and their powders, *Journal of Geophysical Research*, *107*(E4), doi:10.1029/2000JE001462.

Estep-Barnes, P. A. (1977), Infrared Spectroscopy, in *Physical Methods in Determinative Mineralogy*, pp. 529-603, Academic Press.

Glotch, T. D. et al. (2010), Highly silicic compositions on the Moon., *Science*, *329*(5998), 1510-3, doi:10.1126/science.1192148.

Glotch, T. D., B. T. Greenhagen, and P. G. Lucey (2012), Observations of Lunar Swirls by the Diviner Lunar Radiometer Experiment, in *Lunar and Planetary Science Conference*.

Greenhagen, B. T. et al. (2010), Global silicate mineralogy of the moon from the Diviner Lunar Radiometer, *Science*, *329*(5998), 1507-9, doi:10.1126/science.1192196.

Grieve, R. A. F. (1981), Impact cratering, *Nature*, *291*, 16.

Grieve, R. A. F., and P. B. Robertson (1979), The terrestrial cratering record: I. Current status of observations, *Icarus, 38*, 212-229.

Gross, J., and A. H. Treiman (2011), Unique Spinel-Rich Lithology in Lunar Meteorite ALHA81005: Origin and Possible Connection to M3 Observations of the Farside Highlands., *Journal of Geophysical Research*, *116*, 1-9, doi:10.1029/2011JE003858.

Heiken, G. H., D. T. Vaniman, and B. M. French (1991), *Lunar sourcebook: a user's guide to the moon*, Cambridge Univ Pr.

Henderson, B. G., and B. M. Jakosky (1994), Near-surface thermal gradients and their effects on mid-infrared emission spectra of planetary surfaces, *Journal of Geophysical Research*, *99*(E9), 19063-19073, doi:10.1029/94JE01861.

Henderson, B. G., and B. M. Jakosky (1997), Near-surface thermal gradients and mid-IR emission spectra: A new model including scattering and application to real data, *Journal of geophysical research*, *102*(E3), 6567–6580.

Hörz, F., R. A. F. Grieve, G. H. Heiken, P. Spudis, and A. B. Binder (1991), Lunar surface processes, in *Lunar Sourcebook: A User's Guide to the Moon*, edited by G. H. Heiken, D. T. Vaniman, and B. M. French, pp. 61–120, Cambridge University Press.

International Astronomical Union (IAU) Working Group for Planetary System Nomenclature (WGPSN) (n.d.), Gazetteer of Planetary Nomenclature, [online] Available from: http://planetarynames.wr.usgs.gov/

Ishihara, Y., S. Goossens, K. Matsumoto, H. Noda, H. Araki, N. Namiki, H. Hanada, T. Iwata, S. Tazawa, and S. Sasaki (2009), Crustal thickness of the Moon: Implications for farside basin structures, *Geophysical Research Letters*, *36*(19), 1-4, doi:10.1029/2009GL039708.

Jolliff, B. L., M. A. Wieczorek, C. K. Shearer, and C. R. Neal (Eds.) (2006), *New Views of the Moon*, Mineralogical Society of America.

Joy, K. H., I. A. Crawford, S. S. Russell, and A. T. Kearsley (2010), Lunar meteorite regolith breccias: An in situ study of impact melt composition using LA-ICP-MS with implications for the composition of the lunar crust, *Meteoritics & Planetary Science*, *45*(6), 917-946, doi:10.1111/j.1945-5100.2010.01067.x.

Jutzi, M., and E. Asphaug (2011), Forming the lunar farside highlands by accretion of a companion moon, *Nature*, *476*(7358), 69-72, doi:10.1038/nature10289.

Kahle, A. B., F. D. Palluconi, and P. R. Christensen (1993), Thermal emission spectroscopy: Applications to the Earth and Mars, edited by C. M. Pieters and P. A. J. Englert, pp. 99-120, Cambridge University Press.

Korotev, R. L., R. A. Zeigler, and B. L. Jolliff (2009), Compositional and lithological diversity among brecciated lunar meteorites of intermediate iron concentration, *Meteoritics & Planetary Science*, *1322*(9), 1287-1322.

Lawrence, D. J., W. C. Feldman, R. C. Elphic, R. C. Little, T. H. Prettyman, S. Maurice, P. G. Lucey, and A. B. Binder (2002), Iron abundances on the lunar surface as measured by the Lunar Prospector gamma-ray and neutron spectrometers, *J. Geophys. Res*, *107*(E12), doi:10.1029/2001JE001530.

Lucey, P. G. et al. (2006), Understanding the lunar surface and space-moon interactions, *Reviews in Mineralogy and Geochemistry*, *60*, 83-220.

Lucey, P. G., D. Blewett, and G. J. Taylor (2000), Imaging of lunar surface maturity, *Journal of Geophysical Research*, *105*, 377-386.

Lucey, P. G., and B. T. Greenhagen (2012), Lunar Mineral Maps Integrating Thermal and Near Infrared Multispectral Imaging, in *Lunar and Planetary Science Conference*.

Lucey, P. G., B. R. Hawke, and K. Horton (1991), The distribution of olivine in the crater Copernicus, *Geophysical Research Letters*, *18*(11), 2133–2136.

Lucey, P. G., D. A. Paige, B. T. Greenhagen, J. L. Bandfield, and T. D. Glotch (2010), Comparison of Diviner Christiansen Feature Position and Visible Albedo: Composition and Space Weathering Implications, in *Lunar and Planetary Science Conference*, vol. 111.

Melosh, H. J. (1989), *Impact cratering: A geologic process*, Oxford University Press (Oxford Monographs on Geology and Geophysics, No. 11).

Melosh, H. J., and B. A. Ivanov (1999), Impact Crater Collapse, *Annual Review of Earth and Planetary Sciences*, *27*(1), 385-415, doi:10.1146/annurev.earth.27.1.385.

Le Mouélic, S., and Y. Langevin (2001), The olivine at the lunar crater Copernicus as seen by Clementine NIR data, *Planetary and Space Science*, *49*(1), 65-70, doi:10.1016/S0032-0633(00)00091-X.

Le Mouélic, S., Y. Langevin, S. Erard, P. Pinet, S. D. Chevrel, and Y. Daydou (2000), Discrimination between maturity and composition of lunar soils from integrated Clementine UV-visible/near-infrared data: Application to the Aristarchus Plateau, *Journal of geophysical research*, *105*(E4), 9445–9455, doi:10.1029/1999JE001196.

Mustard, J. F., and J. Hays (1997), Effects of Hyperfine Particles on Reflectance Spectra from 0.3 to 25 μm, *Icarus*, *125*(1), 145-163, doi:10.1006/icar.1996.5583.

Mustard, J. F., and C. M. Pieters (1989), Photometric phase functions of common geologic minerals and applications to quantitative analysis of mineral mixture reflectance spectra, *Journal of Geophysical Research*, *94*.

Noble, S. K., C. M. Pieters, L. A. Taylor, R. V. Morris, C. C. Allen, D. S. McKay, and L. P. Keller (2001), The optical properties of the finest fraction of lunar soil: Implications for space weathering, *Meteoritics & Planetary Science*, *36*(1), 31-42, doi:10.1111/j.1945-5100.2001.tb01808.x.

Paige, D. A. et al. (2009), The Lunar Reconnaissance Orbiter Diviner Lunar Radiometer Experiment, *Space Science Reviews*, *150*(1-4), 125-160, doi:10.1007/s11214-009-9529-2.

Paige, D. A. et al. (2010), Diviner Lunar Radiometer observations of cold traps in the Moon's south polar region., *Science*, *330*(6003), 479-82, doi:10.1126/science.1187726.

Pieters, C. M. (1982), Copernicus crater central peak: Lunar mountain of unique composition, *Science*, *215*(4528), 59.

Pieters, C. M. (1986), Composition of the lunar highland crust from near-infrared spectroscopy, *Reviews of Geophysics*, *24*(3), 557-578.

Pieters, C. M. et al. (2009), The Moon Mineralogy Mapper (M3) on Chandrayaan-1, *Current Science*, *96*(4), 1-6.

Pieters, C. M. et al. (2011), Mg-spinel lithology: A new rock type on the lunar farside, *Journal of Geophysical Research*, *116*, doi:10.1029/2010JE003727.

Pinet, P., S. D. Chevrel, and P. Martin (1993), Copernicus: a regional probe of the lunar interior., *Science*, *260*(5109), 797-801, doi:10.1126/science.260.5109.797.

Robinson, M. S. et al. (2010), Lunar Reconnaissance Orbiter Camera (LROC) Instrument Overview, *Space Science Reviews*, *150*(1-4), 81-124, doi:10.1007/s11214-010-9634-2.

Ryder, G., and J. A. Wood (1977), Serenitatis and Imbrium impact melts-Implications for large-scale layering in the lunar crust, in *Lunar and Planetary Science Conference*.

Salisbury, J. W. (1993), Mid-infrared spectroscopy: Laboratory data, *Remote geochemical analysis: Elemental and mineralogical composition*, 79–98.

Salisbury, J. W., G. R. Hunt, and L. M. Logan (1973), Infrared spectra of Apollo 16 fines, *Lunar and Planetary Science Conference*, *4*, 3191.

Shepard, M. K., R. A. Brackett, and R. E. Arvidson (1995), Self-affine (fractal) topography: Surface parameterization and radar scattering, *Journal of geophysical research*, *100*(E6), 11709–11.

Smith, B. G. (1967), Lunar surface roughness: shadowing and thermal emission, *Journal of Geophysical Research*, *72*(16), 4059–4067.

Spencer, J. R. (1990), A rough-surface thermophysical model for airless planets, *Icarus*, *83*(1), 27-38, doi:10.1016/0019-1035(90)90004-S.

Taylor, L. A., C. M. Pieters, L. P. Keller, R. V. Morris, and D. S. McKay (2001), Lunar mare soils: Space weathering and the major effects of surface-correlated nanophase Fe, *Journal of geophysical research*, *106*(E11), 27985–27, doi:10.1029/2000JE001402.

Tompkins, S., and C. M. Pieters (1999), Mineralogy of the lunar crust: Results from Clementine, *Meteoritics & Planetary Science*, *34*(1), 25–41.

Warner, J., C. Simonds, and W. Phinney (1976), Genetic distinction between anorthosites and Mg-rich plutonic rocks: new data from 76255, in *Lunar and Planetary Science Conference*, pp. 915-917.

Wieczorek, M. A. et al. (2006), The Constitution and Structure of the Lunar Interior, *Reviews in Mineralogy and Geochemistry*, *60*(1), 221-364, doi:10.2138/rmg.2006.60.3.

Wieczorek, M. A., and M. T. Zuber (2001), The composition and origin of the lunar crust: Constraints from central peaks and crustal thickness modeling, *Geophysical Research Letters*, *28*(21), 4023, doi:10.1029/2001GL012918.

Yamamoto, S. et al. (2010), Possible mantle origin of olivine around lunar impact basins detected by SELENE, *Nature Geoscience*, *3*(8), 533-536, doi:10.1038/ngeo897.

Zuber, M. T. et al. (2010), The Lunar Reconnaissance Orbiter Laser Ranging Investigation, *Space Science Reviews*, *150*(1-4), 63-80, doi:10.1007/s11214-009-9511-z.

Appendix

Table 2 Central peak compositional results for 135 craters, sorted by descending CF value (most mafic to most felsic). Clementine-derived OMAT and FeO abundance are averaged over the same area that the CF value was sampled. Crustal thickness from Wieczorek et al. [2006]. Central peak depth of origin is $0.109D^{1.08}$*, where D is crater diameter* [*Cintala and Grieve*, 1998]. *Proximity to the crust-mantle interface is the percentage of the crustal column below central peak depth of origin* [*Cahill et al.*, 2009].

	Crater Name	Lat.	Long.	Diameter [km]	Avg CF value [μm]	Avg OMAT	Avg FeO [vol.%]	Crustal thickness [km]	Peak Depth of origin [km]	Proximity to crust-mantle interface [%]
1	Eratosthenes	14.5	348.7	58.8	8.483	0.231	15.213	38.5	8.9	76.924
2	Plummer	-24.7	205.1	67.5	8.421	0.180	10.275	36.1	10.3	71.471
3	Scaliger	-27.3	109.1	86.4	8.391	0.274	11.530	43.3	13.5	68.95
4	Taruntius	5.5	46.5	57.3	8.388	0.207	13.507	46.0	8.6	81.236
5	Barringer	-28.2	209.5	66.9	8.359	0.216	15.203	26.8	10.2	61.911
6	Gutenberg	-8.7	41.2	69.5	8.313	0.176	8.865	56.0	10.6	81.01
7	Plinius	15.3	23.7	42.9	8.296	0.204	10.598	43.3	6.3	85.39
8	Balzac	-8.2	95.0	34.8	8.292	0.193	5.086	54.7	5.0	90.791
9	Icarus	-5.6	187.0	93.7	8.272	0.230	4.945	63.5	14.7	76.881
10	Stratton	-5.8	164.9	69.8	8.262	0.207	4.755	39.0	10.7	72.589
11	Buisson	-1.4	113.3	62.1	8.262	0.203	7.234	61.6	9.4	84.696
12	Da Vinci	9.1	44.9	37.5	8.258	0.193	10.793	54.1	5.5	89.912
13	Albategnius	-11.2	4.0	130.8	8.255	0.194	7.012	56.4	21.1	62.642
14	Agrippa	4.1	10.5	43.8	8.247	0.235	7.502	56.4	6.5	88.56
15	Doppelmayer	-28.5	318.5	65.1	8.241	0.179	15.215	30.4	9.9	67.365
16	Sierpinski	-27.2	155.0	69.1	8.228	0.201	6.893	38.6	10.6	72.65
17	Al Khwarizmi	7.1	107.1	58.6	8.222	0.218	6.180	40.4	8.8	78.116
18	Purbach	-25.6	358.0	119.3	8.215	0.213	8.491	48.3	19.1	60.507
19	Klein	-12.0	2.5	43.5	8.212	0.193	7.596	52.3	6.4	87.759
20	Hilbert	-18.0	108.4	162.6	8.210	0.197	5.674	53.7	26.6	50.416
21	Gavrilov	17.4	131.0	61.6	8.208	0.214	5.372	47.3	9.3	80.241
22	Lohse	-13.7	60.3	43.3	8.208	0.220	8.373	53.1	6.4	87.972
23	Kapteyn	-10.8	70.5	49.5	8.207	0.214	7.016	41.9	7.4	82.392
24	Pannekoek	-4.6	140.7	67.5	8.206	0.216	4.936	64.2	10.3	83.955
25	Behaim	-16.6	79.4	56.2	8.203	0.201	7.132	49.6	8.5	82.943
26	crater 05	-28.6	124.2	38.9	8.196	0.186	6.047	44.4	5.7	87.208
27	Orlov	-25.8	185.2	63.8	8.196	0.246	11.947	18.3	9.7	46.923
28	Cyrillus	-13.3	24.1	98.1	8.191	0.244	5.294	61.1	15.4	74.759
29	Butlerov	12.0	251.2	38.8	8.187	0.246	6.426	47.9	5.7	88.187
30	De Vries	-19.7	183.6	60.3	8.186	0.207	8.490	40.7	9.1	77.56
31	Lansberg	-0.3	333.3	39.8	8.175	0.247	13.998	44.3	5.8	86.844
32	Hubble	22.3	86.9	79.6	8.175	0.224	5.596	48.5	12.3	74.64
33	Neper	8.7	84.6	144.3	8.174	0.171	6.386	37.1	23.4	36.848
34	crater 39	-8.8	184.6	88.1	8.172	0.228	4.252	48.1	13.7	71.415

	Crater Name	Lat.	Long.	Diameter [km]	Avg CF value [µm]	Avg OMAT	Avg FeO [vol.%]	Crustal thickness [km]	Peak Depth of origin [km]	Proximity to crust-mantle interface [%]
35	Glazenap	-2.3	137.7	39.0	8.170	0.244	4.628	71.4	5.7	92.032
36	Brunner	-9.8	90.9	52.7	8.170	0.206	4.997	47.6	7.9	83.435
37	crater 01	-29.0	147.9	73.5	8.169	0.217	6.435	48.5	11.3	76.699
38	Alpetragius	-16.1	355.5	40.0	8.161	0.220	8.565	50.2	5.9	88.33
39	crater 13	7.2	125.5	41.1	8.155	0.221	5.954	57.4	6.0	89.5
40	Siedentopf	22.0	135.1	62.7	8.155	0.211	4.620	54.1	9.5	82.422
41	Joliot	25.7	93.4	169.3	8.153	0.191	6.952	41.8	27.8	33.464
42	La Perouse	-10.6	76.2	80.4	8.152	0.242	6.156	46.1	12.4	72.969
43	crater 17	18.9	135.1	34.4	8.152	0.222	4.859	48.9	5.0	89.806
44	Von der Pahlen	-24.9	227.1	53.9	8.148	0.231	6.056	98.7	8.1	91.813
45	Back	1.3	80.6	34.6	8.148	0.220	7.381	33.0	5.0	84.796
46	Sirsalis	-12.5	299.5	40.2	8.146	0.259	8.599	48.5	5.9	87.852
47	Laue	28.4	262.9	89.2	8.146	0.192	6.712	41.3	13.9	66.292
48	Copernicus	9.6	339.9	96.1	8.143	0.308	6.725	39.5	15.1	61.848
49	Leuschner	1.6	250.9	50.1	8.143	0.236	5.144	48.6	7.5	84.618
50	Keeler	-9.9	162.0	158.1	8.143	0.218	4.361	41.9	25.8	38.325
51	Pitatus	-29.9	346.4	100.6	8.142	0.208	10.069	42.8	15.9	62.919
52	Nobili	0.1	75.9	41.8	8.141	0.172	9.297	56.3	6.1	89.097
53	Vernadskiy	23.1	130.3	92.0	8.137	0.207	5.581	52.6	14.4	72.638
54	crater 19	23.8	114.3	34.6	8.135	0.235	7.291	40.7	5.0	87.712
55	Pontanus	-28.5	14.3	55.7	8.134	0.224	5.327	59.0	8.4	85.806
56	Papaleksi	9.4	164.6	97.7	8.132	0.228	4.081	37.9	15.4	59.45
57	crater 09	-14.6	217.3	43.4	8.132	0.224	6.313	72.2	6.4	91.133
58	Maunder	-14.5	266.2	53.8	8.130	0.268	7.951	29.5	8.1	72.631
59	Borda	-25.2	46.5	47.4	8.127	0.226	5.665	55.5	7.0	87.318
60	Meggers	24.2	122.8	51.2	8.123	0.223	5.579	44.5	7.6	82.845
61	Colombo	-15.3	46.1	79.0	8.117	0.206	5.861	52.9	12.2	76.892
62	Green	3.7	133.2	68.3	8.108	0.203	5.750	63.2	10.4	83.482
63	Arzachel	-18.3	358.0	97.0	8.107	0.252	7.976	54.8	15.2	72.173
64	crater 06	-26.4	68.5	36.0	8.105	0.261	9.760	48.9	5.2	89.312
65	Belyaev	23.0	143.0	53.6	8.100	0.222	4.217	55.5	8.0	85.544
66	Abenezra	-21.0	11.9	43.2	8.092	0.238	4.832	55.3	6.4	88.504
67	crater 02	-24.2	233.6	51.2	8.091	0.263	5.524	98.8	7.6	92.264
68	Airy	-18.2	5.6	38.9	8.090	0.256	6.335	49.1	5.7	88.422
69	Moiseev	9.5	103.3	61.2	8.087	0.268	6.178	48.1	9.3	80.736
70	Necho	-5.2	123.2	33.8	8.085	0.356	7.016	54.6	4.9	91.062
71	crater 33	12.4	100.0	44.1	8.085			54.8	6.5	88.13
72	Ctesibius	1.0	118.6	32.1	8.085	0.279	6.018	51.7	4.6	91.071
73	Cleomedes	27.5	55.5	130.8	8.078	0.249	4.369	50.3	21.1	58.129
74	Tsiolkovskiy	-20.5	129.1	184.4	8.077	0.245	5.116	45.3	30.5	32.578
75	crater 12	5.6	194.3	48.3	8.077	0.235	5.260	58.3	7.2	87.68

	Crater Name	Lat.	Long.	Diameter [km]	Avg CF value [µm]	Avg OMAT	Avg FeO [vol.%]	Crustal thickness [km]	Peak Depth of origin [km]	Proximity to crust-mantle interface [%]
76	Van Vleck	-1.7	78.2	33.5	8.076	0.194	6.481	38.8	4.8	87.54
77	Godin	1.8	10.1	33.6	8.075	0.274	7.642	61.1	4.8	92.067
78	Humboldt	-26.9	80.8	199.5	8.075	0.221	3.906	35.3	33.2	5.8487
79	Theophilus	-11.5	26.3	98.6	8.074	0.283	4.323	33.9	15.5	54.215
80	crater 23	-29.2	145.7	42.7	8.072	0.252	7.621	40.0	6.3	84.29
81	Romer	25.4	36.4	40.8	8.071	0.312	10.386	53.6	6.0	88.838
82	Schuster	4.2	146.4	103.5	8.065	0.220	3.508	51.5	16.3	68.271
83	Langrenus	-8.9	61.0	132.0	8.064			45.5	21.3	53.251
84	Spencer Jones	13.1	166.0	88.2	8.062	0.251	3.971	51.4	13.8	73.257
85	Valier	6.7	174.5	65.1	8.061	0.243	3.742	51.6	9.9	80.807
86	crater 10	-8.5	202.6	54.6	8.059	0.215	4.134	51.2	8.2	84.012
87	crater 08	-22.6	37.2	26.7	8.057	0.215	5.536	50.1	3.8	92.452
88	Sklodowska	-18.1	96.2	125.6	8.056	0.264	6.162	43.6	20.1	53.812
89	Taylor	-5.4	16.6	39.1	8.054	0.223	6.466	60.6	5.7	90.568
90	Bok	-20.2	188.7	43.0	8.053	0.247	11.682	31.5	6.3	79.86
91	Newcomb	29.8	43.7	39.8	8.052	0.226	6.348	53.2	5.8	89.046
92	Seyfert	29.2	114.2	109.8	8.050	0.255	5.834	44.4	17.4	60.731
93	crater 04	4.5	159.8	52.1	8.048	0.236	4.022	51.5	7.8	84.86
94	Manilius	14.4	9.1	37.8	8.046	0.217	6.477	51.7	5.5	89.331
95	crater 15	16.3	173.8	46.7	8.045	0.247	4.307	24.7	6.9	71.984
96	Zernike	18.3	168.2	49.5	8.045	0.242	4.308	38.2	7.4	80.734
97	Lobachevskiy	9.8	113.3	87.7	8.044	0.288	7.166	40.1	13.7	65.877
98	crater 32	7.2	168.7	37.7	8.042	0.256	4.700	48.4	5.5	88.625
99	Ellerman	-25.6	239.5	46.2	8.035	0.222	5.741	64.0	6.8	89.313
100	Lowell	-13.0	256.6	62.7	8.035	0.313	7.419	68.5	9.5	86.127
101	Crookes	-10.4	194.9	49.7	8.033	0.301	5.364	64.9	7.4	88.61
102	Sniadecki	-22.3	191.3	41.1	8.032	0.199	7.055	22.2	6.0	72.798
103	crater 24	-16.6	112.3	45.9	8.032			59.9	6.8	88.665
104	Harvey	19.4	213.4	60.0	8.028	0.242	5.437	66.3	9.1	86.324
105	Eichstadt	-22.7	281.6	50.1	8.028	0.238	6.440	46.1	7.5	83.795
106	Mach	18.1	210.9	187.6	8.024	0.222	5.117	48.5	31.1	35.93
107	Alter	18.7	252.1	64.7	8.024	0.227	5.513	42.6	9.8	76.874
108	Plutarch	24.1	79.0	69.6	8.023	0.270	4.228	45.1	10.7	76.398
109	Poynting	17.6	226.6	128.8	8.020	0.219	5.200	58.0	20.7	64.33
110	Bronk	25.9	225.2	61.6	8.017	0.236	5.053	54.7	9.3	82.94
111	Holetschek	-27.8	151.2	38.9	8.008	0.234	5.760	46.8	5.7	87.86
112	Aitken	-16.7	173.3	137.9	8.008	0.243	4.609	41.1	22.3	45.788
113	Gassendi	-17.5	320.0	109.6	8.002	0.229	7.072	42.1	17.4	58.733
114	crater 43	14.9	163.6	48.6	7.999	0.232	4.323	54.6	7.2	86.775
115	Joule	27.2	215.8	97.5	7.995	0.255	4.032	60.2	15.3	74.527
116	Jackson	22.0	196.8	71.8	7.993	0.383	6.730	64.9	11.0	83.051

	Crater Name	Lat.	Long.	Diameter [km]	Avg CF value [µm]	Avg OMAT	Avg FeO [vol.%]	Crustal thickness [km]	Peak Depth of origin [km]	Proximity to crust-mantle interface [%]
117	crater 16	17.4	277.8	45.9	7.992	0.233	4.860	36.5	6.8	81.391
118	Piccolomini	-29.7	32.2	87.6	7.991	0.236	4.292	53.6	13.7	74.538
119	Ohm	18.3	246.2	63.0	7.988	0.298	8.614	54.9	9.6	82.585
120	Golitsyn	-25.2	254.9	32.7	7.970	0.250	5.491	54.5	4.7	91.355
121	crater 20	26.6	183.0	38.0	7.965	0.280	4.185	53.2	5.5	89.581
122	Sharonov	12.4	173.2	78.2	7.955	0.280	4.260	42.6	12.1	71.637
123	King	5.0	120.4	77.6	7.954	0.372	8.585	49.3	12.0	75.718
124	Robertson	21.8	254.6	89.9	7.942	0.265	5.568	39.0	14.0	64.042
125	Langemak	-9.9	119.5	105.3	7.935	0.284	6.060	50.7	16.7	67.118
126	Buys Ballot	20.8	174.7	66.4	7.933	0.261	4.049	17.5	10.1	42.016
127	crater 37	-27.3	231.9	32.2	7.930	0.234	5.321	83.7	4.6	94.465
128	Alphonsus	-13.4	357.1	110.5	7.891	0.236	4.480	54.3	17.6	67.697
129	Bullialdus	-20.7	337.6	60.7	7.871	0.372	10.920	30.4	9.2	69.758
130	Virtanen	15.8	176.9	44.6	7.862	0.334	3.163	33.1	6.6	80.129
131	Izsak	-23.3	117.6	31.3	7.849	0.263	5.305	51.1	4.5	91.206
132	Petavius	-25.4	60.8	184.1	7.839			45.8	30.4	33.585
133	Olcott	20.4	117.5	79.9	7.833	0.313	3.739	38.4	12.4	67.811
134	Kepler	8.1	322.0	29.5	7.784	0.335	14.134	42.7	4.2	90.122
135	Aristarchus	23.7	312.5	40.0	7.700	0.415	6.260	34.9	5.9	83.234